Comparative analysis of bore propagation over long distances using conventional linear and KdV-based nonlinear Fourier transform

Brühl, Markus; Prins, Peter J.; Ujvary, Sebastian; Barranco, Ignacio; Wahls, S.; Liu, Philip L.-F.
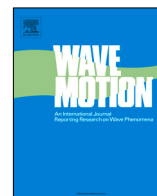
Important note
To cite this publication, please use the final published version (if applicable).
Please check the document version above.

Comparative analysis of bore propagation over long distances using conventional linear and KdV-based nonlinear Fourier transform

Markus Brühl [a],[*], Peter J. Prins [a], Sebastian Ujvary [b], Ignacio Barranco [c], Sander Wahls [a], Philip L.-F. Liu [c]

[a] *Delft Center of Systems and Control (DCSC), Delft University of Technology, Delft, The Netherlands*
[b] *Leichtweiß-Institute for Hydraulic Engineering and Water Resources, Div. of Hydromechanics, Coastal and Ocean Engineering, TU Braunschweig, Braunschweig, Germany*
[c] *Department of Civil and Environmental Engineering, National University of Singapore (NUS), Singapore*

ABSTRACT

In this paper, we study the propagation of bores over a long distance. We employ experimental data as input for numerical simulations using COULWAVE. The experimental flume is extended numerically to an effective relative length of $x/h = 3000$, which allows all far-field solitons to emerge from the undular bore in the simulation data. We apply the periodic KdV-based nonlinear Fourier transform (KdV-NFT) to the time series taken at different numerical gauges and compare the results with those of the conventional Fourier transform. We find that the periodic KdV-NFT reliably predicts the number and the amplitudes of all far-field solitons from the near-field data long before the solitons start to emerge from the bore, even though the propagation is only approximated by the KdV. It is the first time that the predictions of the KdV-NFT are demonstrated over such long distances in a realistic set-up. In contrast, the conventional linear FT is unable to reveal the hidden solitons in the bore. We repeat our analyses using space instead of time series to investigate whether the space or time version of the KdV provides better predictions. Finally, we show how stepwise superposition of the determined solitons, including the nonlinear interactions between individual solitons, returns the analysed initial bore data.

1. Introduction

Experiments show that bores with initial trapezoidal shape transform significantly in shallow water, leading to the generation of undular oscillations at the bore front. Furthermore, numerical simulations and theoretical investigations (e.g. in El [1]) demonstrate that these undulating bores eventually transform into trains of rank-ordered solitons (i.e. "with the largest at the front of the packet and the smallest at its rear" (Apel [2, p. 191], Brühl et al. [3]). The height of the leading, largest soliton above the still water level (SWL) in the far field can be expected to be up to twice of the initial bore height in the far field (El [1, Eq. (70)], Gavrilyuk et al. [4, Fig. 6]). Trailing oscillatory waves may follow the train of solitons and

---

eventually disappear in the far field. Detailed theoretical, experimental and numerical investigations on the evolution of initially bore-shaped waves are given by Hammack and Segur [5] and Osborne [6].

More recent publications have described the shape of observed tsunami events as undular bores (e.g. in Takahashi and Tomita [7]) with significant peak amplification compared to the initial bore height. Furthermore, Madsen et al. [8] show that bore-shaped waves are the most realistic representation to tsunami waves at the shore. They point out that the geophysical scales of ocean basins and continental shelfs are too short to allow soliton separation from the bore front before tsunamis reach the shoreline. On the other hand, field observations in very shallow water conditions such as above fringing reefs show that the disintegration of the initial bore into trains of solitons can occur (e.g. Tissier et al. [9]). Thus, there exist geophysical scales that provide sufficient propagation distance for significant amplification of undular bores, leading to the emergence of solitons. An analysis method for reliably determining the number and amplitudes of the far-field solitons based on the initial near-field bore shape would improve the risk assessment for possibly affected coastal locations.

Parallel to the research advancement in bore generation and propagation, significant improvements have been made in the field of nonlinear wave analysis in recent years. The so-called nonlinear Fourier transform (NFT) or inverse scattering transform (IST) has been enhanced from a rather theoretical mathematical procedure to practical applications in ocean engineering (Osborne [10]). For coastal-engineering applications within shallow waters, the NFT based on the Korteweg–de Vries (KdV) equation, the so-called KdV-NFT, can be applied (Osborne [10], Brühl [11]). The KdV-NFT method is based on the Lax pair of the KdV equation (Gardner et al. [12], Lax [13]) and assumes that the KdV equation governs the propagation of waves in shallow water with $kh < 1.36$ (or $h/L < 0.22$) with wavenumber k, water depth h and wave length L (Osborne and Petti [14, p. 1731], Osborne [15, p. 2629]). The key feature of the periodic KdV-NFT is the nonlinear spectral decomposition of a given periodic free-surface elevation as function of time, $\eta(x_0, t)$ (*time series*), or position $\eta(x, t_0)$ (*space series*) into cnoidal waves. Since cnoidal waves are the solutions of the KdV equation for periodic travelling-wave boundary conditions (Korteweg and De Vries [16]), the periodic KdV-NFT separates the underlying cnoidal waves $\eta_{cn,i}(x, t)$ within the original data from other signal representing their nonlinear wave–wave interactions $\eta_{int,j}(x, t)$. Therefore, the KdV-NFT determines the amplitudes of *all* solitons within the bore, not just the maximum amplitude of the leading soliton that can be obtained from the theory or empirical equations as given in Section 2.4, Eqs. (14) and (15).

Since cnoidal waves are turning into solitons as their modulus approaches the value of one, the nonlinear spectrum can also explicitly identify soliton-like components that are already present in the initial bore-shaped wave, but currently hidden behind the nonlinear interactions. Since the free surface evolves according to the KdV equation, the nonlinear spectrum evolves according to simple rules (for the vanishing case: Gardner et al. [12]; for the periodic case: Dubrovin [17], Dubrovin and Novikov [18]).

In coastal engineering, the periodic KdV-NFT has been successfully applied for the analysis of long-period wave propagation (Brühl [11], Brühl and Oumeraci [19]), of land-slide generated impulse waves (Brühl and Becker [20], Brühl et al. [21]), and of soliton fission over submerged reefs (Brühl and Oumeraci [22], Brühl and Oumeraci [23], Gossel et al. [24]). Recently, Brühl et al. [3] presented preliminary qualitative and quantitative results of a larger number of initial free-surface elevations of non-breaking undular bores propagating in constant depth.

The disintegration of bores into solitons has been shown in several experiments and numerical simulations. A comparison of soliton amplitudes obtained by inspection of experimental far-field data with soliton amplitudes obtained with KdV-NFTs from near-field data is shown by Hammack and Segur [5] and Osborne [6]. As shown in Table 1, their analyses are limited to short bores showing first emerging solitons within the flume length. In all available experimental studies, the propagation length is limited by the flume length. Furthermore, experimental tests usually provide only time series data so that a comparative analysis of time and space series is not available.

In this study, experimental results were used to calibrate a numerical simulation. Using the simulation results, we can observe the bore dynamics over distances that are much longer than those used in previous studies and allow the complete emergence of all solitons from the initial bore. As indicated in Table 1, the physical flumes of these existing studies have a length of up to 440 times the water depth. We extend the flume length numerically to 3061 times the water depth. Therefore, the numerical simulations extend the analysed data range about seven times the experimental flume length. This allows the complete disintegration of a 16 m long initially trapezoidal-shaped bore into solitons. Furthermore, also for the first time, we compare the accuracy of the soliton parameters extracted from initial time series with those from initial space series. For comparison, we also analyse all data with the conventional linear Fourier transform (FT). The spectrogram representations of the results allow easy understanding of the advantages of the nonlinear approach over the conventional FT analysis. Unlike empirical experimental results or theoretical approaches, the algorithm of the periodic KdV-NFT can decompose any periodic wave form in shallow water (i.e. within the KdV regime) into their underlying basic components. It is not limited to specific shapes such as rectangular waves (e.g. as in El [1] or Hammack and Segur [5]) or pre-defined wave theories. Nevertheless, the dynamics underlying the analysed data must approximately satisfy the KdV that requires low directional spread, no dissipation, and no surface tension. Our 1D simulations use the numerical Boussinesq-type solver COULWAVE (Lynett et al. [25]) which considers dissipation within the selected wave breaking model and neglects surface tension (see Section 4).

The main objectives of this study are i) to demonstrate the capabilities of the nonlinear periodic KdV-NFT for analysing the far-field bore data over long distances using experimentally-validated long-distance numerical simulation results, and (ii) to verify if the KdV-NFT analyses of time and space series provide similar results. The goal of this study is to establish

Table 1
Experimental parameters and range of analysed bore data in the given references and within this study (with $(x/h)_{max}$ the maximum relative gauge position for the analysis, $(t\,c_0/h)_{max}$ the maximum relative length of the analysed time series, and $c_0 = \sqrt{g\,h}$ the shallow-water wave celerity). Maximum relative values within this studies apply to the numerical data.

Parameter	Hammack and Segur [5]	Osborne [6]	This study
Experimental flume length	31.6 m	55 m	28.7 m
Wave maker	vertical piston	piston-type	piston-type
Water depth h	0.05 m	0.10 m	0.098 m
Bore length	0.61 m	1.5 m, 5 m	16 m
Bore height	0.05 m	0.018 m, 0.025 m	0.021 m
Effective num. flume length	n/a	10 m	300 m
max (x/h)	400 (exp.)	440 (exp.)	3061 (num.)
max $(t\,c_0/h)$	540 (exp.)	595 (exp.)	4045 (num.)

the nonlinear KdV-NFT as standard tool for the analysis of bore data. In terms of risk assessment, the results will show that the KdV-NFT can reliably predict the far-field structure of the bore from analysis of initial near-field data.

The paper is structured as follows. The theoretical background is established in Section 2. We give short introductions to the KdV-NFT (Section 2.1), to the generation (Section 2.2) and classification (Section 2.3) of bore waves, and to solitons (Section 2.4). For the exemplary analysis within this study, we selected a test from physical experiments that were carried out and analysed preliminary at NUS Hydraulics Laboratory, Singapore (Ujvary [26]). The experimental set-up, the programme and the pre-processing of the experimental data are presented respectively in Sections 3.1–3.3. Section 4 describes the numerical simulations with COULWAVE. The obtained far-field space and time series are comparatively analysed using the conventional fast Fourier transform (FFT) (Section 5) and KdV-NFT (Section 6). Before discussing the nonlinear analysis results in Section 6.2, we introduce the nonlinear spectrum (Section 6.1). The results are presented as spectrograms showing the spectral evolution in time and space, respectively. For the validation of the analysis results, we first investigate the variations within the nonlinear spectra in time and space (Section 7.1). Second, we compare the spectral-domain and time-domain analysis results (Section 7.2) before we, finally, reconstruct the original data by 'nonlinear superposition'[1] of the individual solitons within the inverse transform (Section 7.3). Finally, we compare and discuss the obtained results and give a summary (Section 8).

2. Theoretical background

2.1. Nonlinear Fourier transform based on the Korteweg–de Vries equation

The KdV equation was proposed by Korteweg and De Vries [16] to describe the evolution of the free surface $\eta(x,\,t)$ of long, unidirectional surface waves in shallow-water (with $h/L < 0.22$) in space and time. For the analysis of space series (measured at a fixed timestep t_0) and the Cauchy problem (initial value problem) $\eta(x,\,t_0)$, the space-like KdV (sKdV) equation is applied. The dimensional form of the periodic sKdV is given as (Miles [27, Eq. (3.1)], Osborne [10, Eq. (1.4)], Whitham [28, Eq. (13.99)]):

$$\eta_t + c_0\eta_x + \alpha\eta\eta_x + \beta\eta_{xxx} = 0, \quad \eta(x,\,t) = \eta(x + L_w,\,t), \tag{1}$$

where $\eta(x,\,t)$ is the free surface elevation as a function of space x and time t, $\eta_t = \partial\eta/\partial t$ the vertical velocity of $\eta(x,\,t)$, $\eta_x = \partial\eta/\partial x$ the partial derivative of $\eta(x,\,t)$ in wave direction x, η_{xxx} the third-order partial derivative in space x of $\eta(x,\,t)$, $\alpha\eta\eta_x$ the nonlinear convective term and $\beta\eta_{xxx}$ the dispersive term. Since periodic travelling-wave conditions are assumed, $\eta(x,\,t) = \eta(x + L_w,\,t)$, the variable x is considered within the interval $0 \leq x \leq L_w$. The wave celerity or linear phase speed in shallow-water c_0, the coefficients α for nonlinearity, β for dispersion and the relation λ between nonlinearity and dispersion are constant parameters that depend on the particular physical application (Osborne [10, Sect. 10.1, p. 219]). For progressive surface waves modelled by the sKdV, these coefficients depend on the water depth h_0 and the acceleration due to gravity g as follows.

$$c_0 = \sqrt{gh_0}, \quad \alpha = \frac{3c_0}{2h_0}, \quad \beta = \frac{c_0h_0^2}{6}, \quad \lambda = \frac{\alpha}{6\beta} = \frac{3}{2h_0^3}. \tag{2}$$

For the analysis of periodic time series (measured at a fixed position x_0) and the boundary value problem $\eta(x_0,\,t)$, the time-like KdV equation (tKdV) is applied, which is obtained from the sKdV equation by changing the space and time variables: $x \to t$ and $t \to x$, $k \to \omega$ and $\omega \to k$ (Osborne [29], Karpman [30]):

$$\eta_x + c_0'\eta_t + \alpha'\eta\eta_t + \beta'\eta_{ttt} = 0, \quad \eta(x,\,t) = \eta(x,\,t + T_w), \tag{3}$$

---

[1] 'Nonlinear superposition' within the context of KdV-NFT means the linear superposition of the nonlinear cnoidal waves and their nonlinear wave–wave interactions within the inverse KdV-NFT. The nonlinear superposition of the spectral results as obtained from direct KdV-NFT returns the original data. The linear superposition of only the spectral components (cnoidal waves) without their interactions will not provide the initial data.

with the modified time-domain coefficients from Eq. (2):

$$c_0' = \frac{1}{c_0} = \frac{1}{\sqrt{gh_0}}, \quad \alpha' = -\frac{\alpha}{c_0^2}, \quad \beta' = -\frac{\beta}{c_0^4}, \quad \lambda' = \frac{\alpha'}{6\beta'} = \frac{3c_0^2}{2h_0^3}. \tag{4}$$

For the solution of the tKdV equation with periodic boundary conditions the signal is considered to be periodic with period T_w. Despite the similar notation and the change of the variable, the space-like KdV is only approximately equivalent to the time-like KdV (see Karpman [30, p. 64], Osborne [6, p. 251]).

The KdV equation is a partial differential equation that can be solved by various methods, depending on the desired purpose and application. Solitary wave solutions as discussed in Antonova and Biswas [31] or Girgis and Biswas [32] provide translatory solitons as solutions. By application of a mathematical procedure called inverse scattering transform (IST) (IST in general: Gardner et al. [12], periodic IST: Novikov [33]), the KdV equation can be solved also for periodic travelling-wave boundary conditions in terms of so-called cnoidal waves. Due to the analogy of this method compared to the application of conventional Fourier transform (FT), the solution of the KdV equation by application of the IST is called KdV-based nonlinear Fourier transform (KdV-NFT). In engineering terminology, the IST of the KdV equation might be considered as an extension or as a substitute of the conventional linear FT by a generalization of the linear Fourier transform for shallow-water waves (Osborne [10, p. xxiii]). For initial conditions $\eta(t, x_0)$ in the linear regime (the small-amplitude limit), the nonlinear KdV reduces to a linear PDE. In this case, the KdV-NFT provides approximately the same results as the conventional FT.

Since the KdV-NFT is based on the KdV equation, it provides physically meaningful results only for free-surface waves that satisfy $kh \leq 1.0$, which describes the range of validity of the KdV equation. With regard to the nonlinear interactions, for practical applications this value can be extended to $kh < 1.36$ ($h/L < 0.22$) (Osborne and Petti [14, p. 1731], Osborne [15, p. 2629]). Larger than these values, the nonlinear wave–wave interactions are governed by the nonlinear Schroedinger equation and no longer by KdV equation (Osborne [10]).

The most important and fascinating feature of the KdV-NFT is the following: With the help of the KdV-NFT we can obtain a representation of the whole wave field given only one time series $\eta(x_0, t)$ or one space series $\eta(x, t_0)$. For periodic travelling-wave solutions, this approach represents the free surface $\eta(x, t)$ as a linear superposition of N constitutive nonlinear cnoidal wave components $\eta_{cn,i}(x, t)$ plus their nonlinear wave–wave interactions $\eta_{int}(x, t)$ (after Osborne [34, Eq. (2.4)], Osborne [10, Eq. (1.8)]):

$$\eta(x, t) = \underbrace{\sum_{i=1}^{N} \eta_{cn,i}(x, t)}_{\substack{\text{linear superposition} \\ \text{of } N \text{ cnoidal waves}}} + \underbrace{\eta_{int}(x, t)}_{\substack{\text{all nonlinear interactions} \\ \text{between the } N \text{ cnoidal waves}}}. \tag{5}$$

The decomposition process of finding the wave parameters for each of the N cnoidal waves $\eta_{cn,i}(x, t)$ from the free surface $\eta(x, t)$ is called the direct KdV-NFT (dKdV-NFT). The nonlinear superposition of these cnoidal waves in the inverse nonlinear Fourier transform (iKdV-NFT), including the calculation of the nonlinear interactions according to (5), returns the original signal $\eta(x, t)$. The interaction term $\eta_{int}(x, t)$ in (5) is not provided by the dKdV-NFT, but is calculated within the iKdV-NFT (see Brühl and Oumeraci [35]).

Due to the nonlinear interactions, the underlying spectral structure of this set of cnoidal-wave basic components cannot be obtained from the free surface elevation $\eta(x, t)$ by time-domain analysis (except for $N = 1$). By application of the KdV-NFT the following parameters can be obtained: The number N of the determined cnoidal waves, their moduli m_i, amplitudes a_i, wave numbers k_i or frequencies ω_i or f_i, and phases φ_i. For details see Osborne [10] and Brühl [11]. Based on the determined values of m_i, the cnoidal waves can be classified as oscillatory waves (for $m_i \leq 0.99$) with the values a_k, k_k, ω_k or f_k (with $f_k = \omega_k/2\pi$) and φ_k, or solitons[2] (for $m_i > 0.99$) with A_j, K_j, Ω_j or F_j (with $F_j = \Omega_j/2\pi$) and Φ_j. In order to better distinguish between oscillatory waves and solitary waves (solitons), the parameters of the solitary waves are denoted by capital letters. The definitions of the wave parameters are given in the Appendix. An example of a nonlinear spectrum is given in Fig. 11 and described in Section 6.1. Further details on the mathematical and numerical background of the methods are given in Osborne [10], Brühl [11] and Brühl and Oumeraci [36].

Note that the KdV-NFT is very versatile since cnoidal waves incorporate all classic wave theories (Airy, Stokes and solitary waves). Hence, it can be applied to various types of free-surface wave data in coastal engineering.

In addition to the cnoidal-wave representation given above, the general spectral solution to the periodic sKdV can also be written as a linear superposition of so-called hyperelliptic functions $\mu_i(x, t)$ (Osborne [10, p. 220, Eq. (10.6)]):

$$\lambda\eta(x, t) = -E_1 + \sum_{N}^{i=1} [2\mu_i(x, t) - E_{2i} - E_{2i+1}], \tag{6}$$

---

[2] By definition, a *soliton* is a translatory wave of permanent shape. Within the context of the periodic KdV-NFT, highly nonlinear cnoidal waves with modulus $m > 0.99$ are similar to solitons. They are periodic, but within the analysed time or space window they provide the typical soliton characteristics with only one crest and no trough. This crest has nearly the same shape, size and celerity as a soliton of the sKdV or tKdV, respectively, with the same amplitude A (see Eqs. (10) and (12)). For brevity, we also refer to cnoidal waves with modulus $m \geq 0.99$ as solitons from here on.
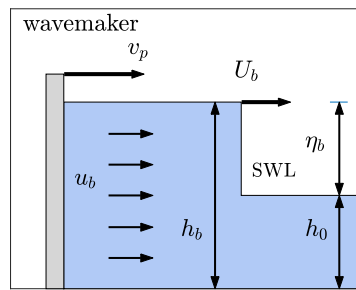
Fig. 1. Definition of key parameters for bore accumulation during constant velocity of the paddle.

with λ as in Eq. (2). The $E_i (1 \leq i \leq 2N + 1)$ are constant eigenvalues that are derived by the KdV-NFT algorithm. The hyperelliptic functions can be considered as a less complicated intermediate step towards the cnoidal-wave representation in Eq. (5). The μ-functions already provide the information about the solitons in the wave field (Osborne [10, Ch. 17.7, p. 446]).

2.2. Generation of bores in wave flumes

Bores in wave flumes can be generated by pushing a still-water body by a wave paddle with velocity v_p, as shown in Fig. 1. The horizontal flow velocity u_b under the bore is assumed to be constant over the vertical plane (Stoker [37, p. 316]) and equal to the wave-paddle velocity ($u_b = v_p$). For the generation of trapezoidal-shaped bores, the paddle is linearly accelerated from $v_p = 0$ to $v_p = u_b$ (with u_b according to the target Froude number $\text{Fr}_{b,\text{nom}}$ in Eq. (8)), then moves with constant velocity, and finally is decelerated back to $v_p = 0$. During the acceleration and deceleration phase of the paddle, the sloped bore front and back are generated, and the constant motion generates the bore plateau. The length of the bore corresponds to the length of the bore plateau. The initial bore (or discontinuity) with height η_b propagates in still-water with initial depth h_0 with constant bore-front celerity U_b (Stoker [37, Sect. 10.6]). The relation between the bore height h_b over the bottom and the bore height η_b over SWL is $h_b = (\eta_b + h_0)$ (see Fig. 1).

Within this study, the propagation of the free surface is characterized by the strength of the bore in terms of the dimensionless bore Froude number Fr_b (Stoker [37], Liggett [38, Sect. 8.4.2])

$$\text{Fr}_b = \frac{U_b - u_0}{\sqrt{gh_0}}, \tag{7}$$

with g the acceleration due to gravity, U_b the bore-front celerity, and u_0 the initial fluid velocity at initial depth h_0. Note that a Froude number $\text{Fr}_b > 1$ is required for the formation of a bore.

The required paddle velocity $v_p = u_b$ for the target Froude number $\text{Fr}_{b,\text{nom}}$ is (Liggett [38, Eq. (8.124)])

$$\frac{u_b}{c_0} = \text{Fr}_{b,\text{nom}} \frac{\sqrt{1 + 8\,\text{Fr}_{b,\text{nom}}^2} - 3}{\sqrt{1 + 8\,\text{Fr}_{b,\text{nom}}^2} - 1}. \tag{8}$$

With the measured depths in front of and under the bore, h_0 and h_b, the actual bore Froude number Fr_b can be calculated employing the bore relations from the measured and simulated data as (after Liggett [38, Eq. (8.123)])

$$\text{Fr}_b = \sqrt{\frac{1}{2}\left(\frac{h_b}{h_0} + \frac{1}{2}\right)^2 - \frac{1}{8}}. \tag{9}$$

While Eq. (9) is derived under the assumption that the bore front is breaking, Barranco and Liu [39] showed that the bore relations also provide good estimations for undulating bores.

2.3. Classification of bores

The properties of propagating bores can be characterized based on the bore relation h_b/h_0 or the bore Froude number Fr_b in Eq. (7). In literature, usually Fr_b is used to define three different types of bore waves as described by Miller [40, p. 4506]: (i) *Undulating bores*, also called waves of translation or Favre waves[3], show values $\text{Fr}_b \leq 1.25$ to 1.27. (ii) *Fully developed* or *breaking bores* are described for values $\text{Fr}_b \geq 1.55$. (iii) *Undulating-breaking bores* are obtained when bores

---

[3] Favre [41, Ch. 7] was the first to show the phenomenon of undular bores in experimental tests.

start to break but still have undulations ($1.25 \leq \mathrm{Fr}_b \leq 1.55$). Similar limits were observed recently by Barranco and Liu [39]. Analytical definitions of limits for the bore regimes require further research.

In this study, experimental and numerical data from an undulating non-breaking bore with nominal bore Froude number $\mathrm{Fr}_{b,\mathrm{nom}} = 1.20$ are analysed in order to validate the ability of the KdV-NFT to determine the far-field solitons from near-field data.

2.4. Solitary waves and their connection to undular bores

The solitary wave (or soliton) is a translatory wave (Russell [42, Tab. 1]) of permanent shape with only one crest and no trough. The solitons we consider in this paper are solutions to the KdV equation. The soliton solution of the sKdV, written as a function of the soliton amplitude A[4] above SWL and the phase Φ, with the constants h_0 and g for water depth and acceleration due to gravity, respectively, is (after Dean and Dalrymple [43, Eqs. (11.84) and (11.81)], Osborne [10, Ch. 1.2.2])

$$\eta(x,\ t) = A \operatorname{sech}^2 \left[\sqrt{\frac{3A}{4h_0^3}} x - \sqrt{\frac{3Ag}{4h_0^2}} \left(1 + \frac{A}{2h_0} \right) t - \Phi \right]. \tag{10}$$

The wave number and the angular frequency as obtained from Eq. (10) for the sKdV are $K = \sqrt{3A/(4h_0^3)}$ and $\Omega = \sqrt{3Ag/(4h_0^2)}(1 + A/(2h_0))$, respectively. x and t are the variables for position and time.

The nonlinear wave celerity C of a soliton in the sKdV is (after Dean and Dalrymple [43, Eq. (11.81)], Osborne [10, Ch. 1.2])

$$C = \frac{\Omega}{K} = c_0 \left(1 + \frac{A}{2 h_0} \right), \tag{11}$$

where $c_0 = \sqrt{gh_0}$ is the wave celerity in shallow water.

For the tKdV, the soliton solution as a function of the wave parameters A and Φ, and the constants h_0 and g is

$$\eta(x,\ t) = A \operatorname{sech}^2 \left[\sqrt{\frac{3A}{4h_0^3}} \left(1 - \frac{A}{2h_0} \right) x - \sqrt{\frac{3Ag}{4h_0^2}} t - \Phi \right]. \tag{12}$$

Here, the wave number and the angular frequency as obtained from Eq. (12) for the tKdV are $K = \sqrt{3A/(4h_0^3)}(1 - A/(2h_0))$ and $\Omega = \sqrt{3Ag/(4h_0^2)}$, respectively.

After interactions with other wave packets, solitons regain their old shapes once the interactions have ceased (Ablowitz and Kodama [44]). Thus, if an initial bore-shaped free-surface near-field signal contains N_{sol} hidden solitons, then in the far field and after a particular time, these solitons emerge from the undulating non-breaking bore and form a train of solitons with different amplitudes (Lamb [45, p. 52]) (e.g. as in Hammack and Segur [5, Fig. 3] and Osborne [6, Fig. 3]). Due to the amplitude dispersion of the solitons (see Eq. (11)), the wave celerity increases with their height, and the larger solitons leave the bore behind earlier than the lower ones and become visible as discrete rank-ordered solitons without significant interactions (see e.g. Figs. 5 and 6). That is, after a sufficiently long time t, the resulting free surface from the N_{sol} separated solitons can be written for the tKdV as (after Prins and Wahls [46, Eq. (4)], Schuur [47]):

$$\eta(x,\ t) \approx \sum_{j=1}^{N_{\mathrm{sol}}} A_j \operatorname{sech}^2 \left[\sqrt{\frac{3A_j}{4h_0^3}} \left(1 - \frac{A_j}{2h_0} \right) x - \sqrt{\frac{3A_j g}{4h_0^2}} t - \Phi_j \right]. \tag{13}$$

For the asymptotic solution in the far field (without the oscillatory tail), the amplitude A_1 of the leading soliton cannot exceed twice the maximum initial free surface elevation $\eta(x,\ t_0)$ at any timestep t_0 (El [1, Eq. (70)], Segur [48, p. 732]):

$$A_1 < 2 \max(\eta(x,\ t_0)). \tag{14}$$

In case of sufficiently long and high bores with initial bore height η_b, the final far-field amplitude A_1 of the leading, largest soliton can be expected to be (El [1, Sect. 3.8], Galindo and Pascual [49, Sect. 4.3], Giovanangeli et al. [50, Sect. II.B], Osborne [51, Sect. 8], Prins and Wahls [52, Sect. 5.3]):

$$A_1 \approx 2 \eta_b = 2 (h_b - h_0), \tag{15}$$

where A_1 is the amplitude of the first, leading soliton in the far field that has already completely emerged from the bore front, η_b the height of the initial trapezoidal-shaped bore before the undulations start to develop, h_b is the depth under the bore, and h_0 is the initial depth in front of the bore (see Fig. 1).

---

[4] Note that for solitary waves that have no wave trough the wave amplitude A is identical with the wave height H, thus $A = H$.
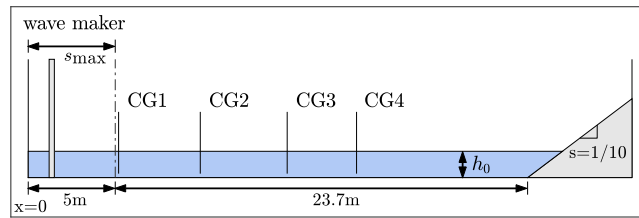
Fig. 2. Experimental set-up in the wave flume at NUS with wave gauges CG1 to CG4 at positions $x = 5.193$ m, 9.887 m, 14.882 m, and 18.869 m.

3. Experimental set-up, programme and data pre-processing

3.1. Experimental set-up

We conducted a set of bore experiments with different strengths and different water depths in the wave flume at the Hydraulic Engineering Laboratory at National University of Singapore (NUS) (see Fig. 2). The wave flume has a length of 36 m, and both width and height are 0.9 m. The flume is equipped with a piston-type wave maker with a stroke of $s_{max} = 5$ m, maximum velocity of $v_{max} = 2.5$ m/s, and maximum acceleration of $a_{max} = 3.5$ m/s^2 that allows the generation of long-period waves and bores (Barranco [53, Sect. 3.3]).

The bores are generated by accelerating the piston-type paddle from the initial position x_i at rest with a constant acceleration a to the desired paddle velocity v_p, then moving the paddle with the constant velocity over a period of time, and finally decelerating the paddle with a deceleration $d = -a$ until it stops. Thus, a trapezoidal shape of the initial free surface is generated. We measured the generated surface displacement of the propagating bore with four capacity gauges CG1 to CG4 at positions $x = 5.193$ m, 9.887 m, 14.882 m, and 18.869 m (see Fig. 2), with CG1 being located 0.193 m behind the maximum-stroke position of the wave paddle. Since the focus of this study is the investigation of the propagation and fission of an incident non-breaking bore, the gauge positions and the time frame for the data analysis are selected such that only the incident bore without reflection from the end of the flume is considered.

3.2. Experimental programme

The experiments generated a total of 44 different bores. A first systematic analysis of the 19 bores with acceleration $a_{nom} = 0.1$ m/s^2 using KdV-NFT has been presented in Brühl et al. [3]. In that study, we have analysed the leading-bore amplitudes for non-breaking and breaking bores with different strengths in different water depths in order to validate the KdV-NFT results for non-breaking bores, and to show the limitations of wave breaking on the spectral results.

In the present study, we selected experiment No. 20 with a non-breaking undular bore for the exemplary and detailed discussion of the application of KdV-NFT to the bore data. The nominal values of the selected experiment are: $Fr_{b,nom} = 1.20$, $s_{nom} = 4$ m, $v_{p,nom} = 0.249$ m/s, $h_{0,nom} = 0.1$ m, $a_{nom} = 0.1$ m/s^2, $d_{nom} = -0.1$ m/s^2. The wave-paddle velocity $v_{p,nom}$ has been calculated by Eq. (8) based on the nominal bore Froude number $Fr_{b,nom}$ and the nominal water depth $h_{0,nom}$.

3.3. Data pre-processing

Before applying the analysis algorithms, we shifted the zero-level of the test data to the mean elevation of the first two seconds of each signal ('zero correction', see Fig. 3) in order to let the elevations start at SWL. Then we applied the so-called time-domain Savitzky–Golay filter (Orfanidis [54]) in order to remove possible temporary high-frequency noise (e.g. by occasional vibration of the wave gauge). Since the KdV-NFT algorithm turned out to be sensitive to small variations in the calibration factors of neighbouring gauges during our analysis, we scaled all data to compensate for these variations. In detail, we assumed that the volume of the bore that passed the four close-by gauges is a constant and integrated the positive bore elevations over time. We then determined the two gauges with the least deviation and defined the mean value at these two gauges as the target value. Finally, we scaled the elevations at all four gauges with respect to the target value. The integration results for the selected experiment No. 20 show a difference of about -2.5% between the lowest value at CG4 compared to the maximum value at CG3. Finally, we scaled the elevations at CG1 to CG4 by factors 1.0137, 1.0009, 0.9991 and 1.0252, respectively. Thus, scaling in experiment No. 20 provides only relatively small changes in the data. Nevertheless, we apply scaling to all data as part of the standard pre-processing for the bore data before applying linear and nonlinear frequency domain analyses. Note that the still water level below the threshold value (here: $\eta \geq 0.0005$ m) before the bore front and after the bore tail is excluded from the scaling. Finally, we used the filtered and scaled data as basis for further pre-processing and the subsequent analyses within this study.

In the next step, we first defined time frames to eliminate reflected and re-reflected waves from the incident bore (see Fig. 3) and truncated the data after the bore tails. Furthermore, for the comparative analysis within this study, we
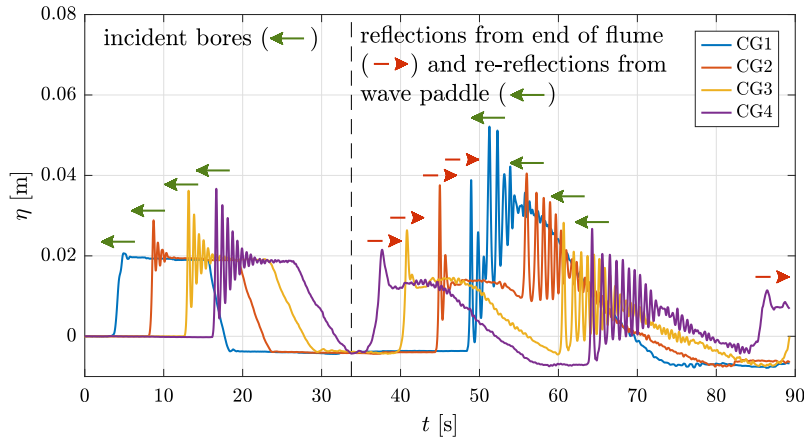
Fig. 3. Imported free-surface data of experiment No. 20 (with nominal values $h_{0,\text{nom}} = 0.10\,\text{m}$, $s_{\text{nom}} = 4\,\text{m}$, $a_{\text{nom}} = 0.1\,\text{m/s}^2$, $d_{\text{nom}} = -0.1\,\text{m/s}^2$, and $v_{\text{nom}} = 0.249\,\text{m/s}$), recorded at wave gauges CG1 to CG4, after zero correction of the data by mean of time interval $0 \leq t \leq 2\,\text{s}$. For $t \lesssim 33\,\text{s}$, the plot shows the incident bores, followed by waves that are reflected at the end of the flume and, finally, re-reflections from the paddle. Green left-pointing arrows indicate bore propagation down the flume, red right-pointing arrows show bores propagating back to the wave maker. (For interpretation of the references to colour in this figure legend, the reader is referred to the web version of this article.)

neglect the negative depression behind the bore since it is caused by the sudden stop of the wave maker, and concentrate on the propagation and evolution of the positive elevations of the bore ($\eta > 0$). After replacing the truncated sections by zeros and rounding off the generated sharp edges by a spline interpolation, we adjust the number of zeros to ensure that all four gauge data within one experiment are given the same duration T_w and number of samples. Fig. 4 shows the final results after pre-processing for experiment No. 20: The blue curves show the pre-processed original data after zero correction, filtering and scaling, the red curves represent the sections where negative elevations have been truncated and replaced by zeros. Note that in this approach we ignore the effect of the trough on bore propagation and soliton fission. Numerical simulations of these experiments with and without trough had shown that the presence of the trough does not affect the leading undulations and large solitons at the bore front. At the bore back, the trough affects the soliton evolution and leads to smaller soliton amplitudes than without trough. Therefore, we can assure that the consideration of only the positive elevation of the bore does not affect the results for the leading, hazardous solitons at the bore front.

4. Numerical simulations of far-field bore propagation

The experimental results in Fig. 3 clearly show that the propagating bore undulates from gauges CG1 to CG4, and that clear peaks are observed at the bore front. Unfortunately, due to the limited length of the wave flume the separation of discrete solitons at the bore front cannot be observed experimentally before the bore is reflected at the slope at the end of the flume. Therefore, we used the numerical model COULWAVE (Lynett et al. [25]) to numerically propagate the incident bore. The numerical model uses a finite-volume scheme for spatial discretization and a 4th-order iterative predictor–corrector scheme for the time integration. By introducing the pre-processed experimental data from gauge CG1 as input time series at the left boundary, we numerically reproduced the experiment (see Fig. 4a).[5] For the numerical simulation, we introduce a new reference frame with time t' and shifted space x'. The definitions of the different variables are given in Table 2. In order to obtain complete separation of the initial bore into solitons, the bore is propagated numerically up to a distance of $x' = 500\,\text{m}$ to allow the complete far-field train of solitons to pass the position $x' = 300\,\text{m}$ (effective flume length, relative distance $x'_0/h = 3061$, with depth $h = 0.098\,\text{m}$ and x'_0 the gauge position in the numerical simulation, where $x' = 0$ corresponds to the location of CG1). The time-series data are obtained at 206 numerical gauges in the COULWAVE simulation of experiment No. 20 in the interval $x' = [0.01\,\text{m}, 400\,\text{m}]$[6] with sampling rate $\Delta t' = 0.0075\,\text{s}$ (with t' the time in the numerical simulation). The space-series data are calculated within COULWAVE at 1001 timesteps within the interval $t' = [0\,\text{s}, 500\,\text{s}]$ with sampling rate $\Delta t' = 0.5\,\text{s}$. The spatial resolution is $\Delta x' = 0.0098\,\text{m}$. In this

---

[5] The numerical simulations as presented in Figs. 5 and 6 are conducted with the following internal settings: (i) using the one-layer model that is referred to as the 'fully nonlinear, extended Boussinesq equation', (ii) fully nonlinear simulation, (iii) weakly rotational model, (iv) finite volume solver with, (v) wave generation using the pre-processed free-surface time-series data of gauge CG1 from Fig. 4a as the input data, (vi) wave-modification factor remaining at the value 1, (vii) the number of grid points per wavelength set as 100, and the Courant number set as 0.25, (viii) the length of the numerical flume is set to 500 m in order to provide sufficient propagation length, (xi) transport-based wave breaking model is used, (x) friction is neglected, and (xi) we iterated the input data based on the simulation results for $x' = 0.01\,\text{m}$ until the target data were met at this position.

[6] The numerical gauges are located at $x' = 0.01\,\text{m}$ (called CG1'), 0.05 m, from 0.5 m to 4.5 m in steps of $\Delta x' = 0.5\,\text{m}$, at locations CG2' to CG4' at 4.694 m, 9.689 m and 13.676 m, respectively, at 15.0 m and from 20.0 m to 400.0 m in steps of $\Delta x' = 2.0\,\text{m}$.
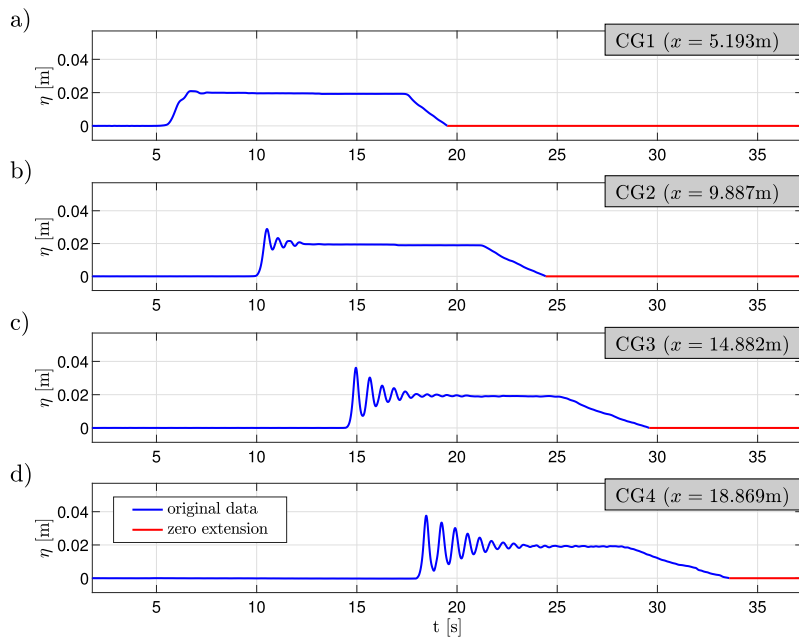
Fig. 4. Pre-processed free surface at CG1 to CG4 from experiment No. 20 after cutting and replacing the negative elevations: Original samples after zero correction, filtering and scaling (blue lines) extended by zeros (red lines) in order to eliminate negative elevations at the back of the bore and to provide identical sample numbers in the data. (For interpretation of the references to colour in this figure legend, the reader is referred to the web version of this article.)

section, we give a short description of the numerical results. For further details on COULWAVE and the internal settings see Lynett et al. [25].

Since we used the data at gauge CG1 (measured at $x = 5.193$ m in the wave flume) as input for the wave generation at position $x' = 0$ in the numerical model, all numerical gauges are shifted by 5.193 m. Thus, the locations of the three numerical gauges CG2', CG3' and CG4' are $x' = 4.694$ m, 9.689 m and 13.676 m, respectively. An additional numerical gauge, denoted as CG1', is placed at $x' = 0.01$ m to allow comparison of the generated surface elevation with the target input data. The small difference in position of CG1 and CG1' is neglected in the following. The down-wave propagation of the bore is captured by additional numerical wave gauges that are placed in the far field starting at $x' = 20$ m until $x' = 400$ m with spacing $\Delta x' = 2$ m.

The comparison in Fig. 5 presents the pre-processed experimental gauge data for CG1 to CG4 (blue curves) from Fig. 3 and the numerical data (red curves) for the gauges CG1' to CG4', respectively. The simulation results clearly show that COULWAVE reliably simulates the behaviour of the bore in the near field as measured at the experimental wave gauges. The only deviations we observed are small time shifts and decreased peak elevations of the leading undulations at gauges CG2' and CG3'. At CG4', these deviations are not present anymore. Therefore, we consider these small variations to be negligible for the following analyses and assume that COULWAVE is reliably simulating the bore propagation from near field to far-field locations.

After we have seen the development of undulations from gauges CG1 to CG4 in the previous figures, Fig. 6 presents the simulation results of experiment No. 20 at selected far-field gauges at positions $x' = 100$ m, 200 m and 300 m. The far-field simulations clearly show that the undulations at the bore front in the near-field data evolve into discrete solitons until the initial bore is completely consumed. In Fig. 6a at position $x' = 100$ m, the solitons have not completely separated yet and the troughs between successive solitons still show elevations significantly larger than zero. At position $x' = 200$ m in Fig. 6b, the solitons 2 to 8 have not completely separated yet. Finally, in Fig. 6c at $x' = 300$ m all solitons have completely evolved out of bore and propagate individually without being significantly affected by mutual interactions. Due to amplitude dispersion of the propagating solitons, the width of the soliton train is further increasing and the trough elevations are close to zero, as can be seen by from Fig. 6a to Fig. 6c.

The time- and frequency-domain analyses that we will discuss in the next sections are obtained by applying the different methods on the numerical COULWAVE simulation data of experiment No. 20.

5. Linear frequency-domain analysis of the bore data

In this section we apply the fast Fourier transform (FFT) as a linear frequency-domain analysis method on both time and space series from the numerical simulation data. Selected numerical time-series data were already presented in Figs. 5
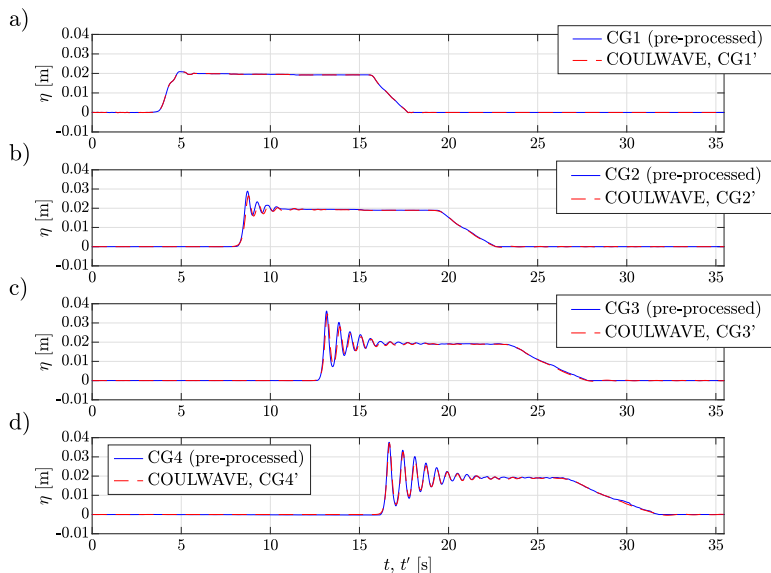
Fig. 5. Comparison of pre-processed near-field data $\eta(x_0, t)$ for experiment No. 20 obtained from gauges CG1 to CG4 (filtered and scaled data with zero extension, blue lines) and $\eta(x'_0, t')$ from numerical simulation gauges CG1' to CG4' (red lines) at numerical flume positions $x' = 0.01\,\mathrm{m}$, 4.694 m, 9.689 m and 13.676 m. (For interpretation of the references to colour in this figure legend, the reader is referred to the web version of this article.)
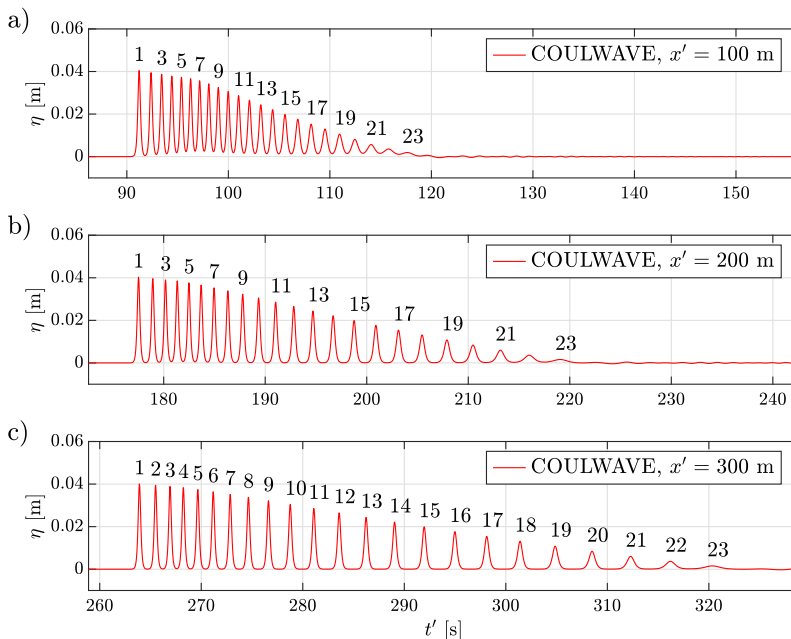

Fig. 6. Numerical far-field simulation data for experiment No. 20 at numerical locations $x' = 100\,\mathrm{m}$, 200 m and 300 m, showing 23 solitons evolving out of the initial bore from Fig. 5.

and 6. In Section 6, we will compare the results obtained in this section with the results from nonlinear frequency-domain analysis with the periodic KdV-NFT.

For the frequency-domain analyses we define a new reference frame with time $\tilde{t}$ and space $\tilde{x}$, respectively, that moves with the initial bore-front celerity U_b (see Figs. 7 and 8).[7] The definitions of the different variables are given in Table 2.

---

[7] In KdV analysis, usually 'retarded' time and space frames are used that move with $c_0 = \sqrt{gh_0}$ because then the second component of the KdV equation vanishes. As a result, all solitons propagate faster than the retarded frame. In contrast, the selection of U_b as reference celerity within this study allows (more descriptive) positive and negative relative celerities of the solitons compared to U_b. Nevertheless, the selection of the reference celerity will not affect the KdV-NFT analysis results.

Table 2
Definition of time and space variables in the experimental data, the numerical simulations, and the moving analysis windows.

| Name	Symbol	Definition
Absolute position	x	Zero at paddle
Absolute time	t	Zero 3.77 s before bore arrives at CG1.
Simulation frame position	x'	$x' = x - 5.193\,\text{m}$
Simulation frame time	t'	$t' = t$
Position at which the nth time series is taken (position of the numerical gauge).	x_0'	The time series is $\eta(t', x_0')$. Value depends on the time series!
Time point at which the nth space series is taken.	t_0'	The space series is $\eta(t_0', x')$. Value depends on the space series!
Moving frame position of the nth space series	$\tilde{x}$	$\tilde{x} = x' - t_0' U_b + 80.18\,\text{m}$
Moving frame time of the nth time series	$\tilde{t}$	$\tilde{t} = t' + 6.23\,\text{s} - x_0'/U_b$, $U_b = 1.136\,\frac{\text{m}}{\text{s}}$
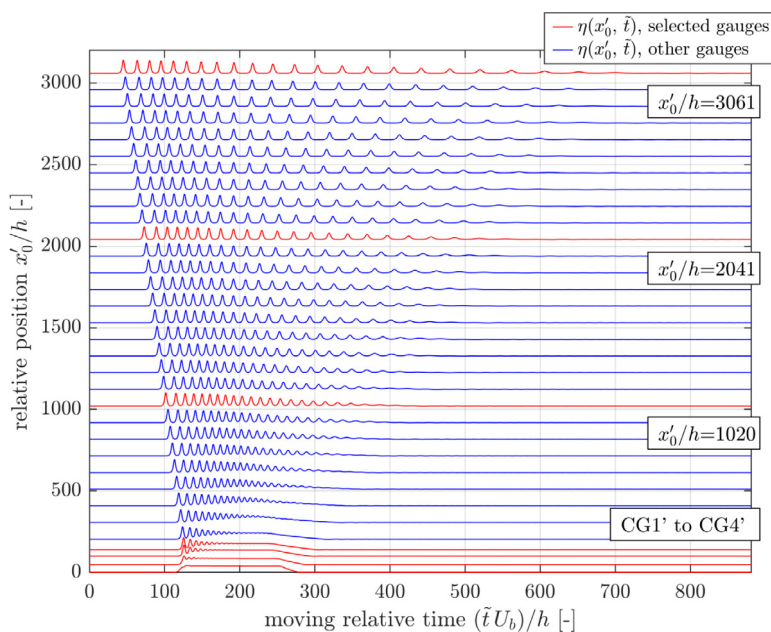
Fig. 7. Spatio-temporal evolution of the free surface time-series $\eta(x_0', \tilde{t})$ of the initial bore of experiment No. 20 from COULWAVE simulation, plotted over moving relative time $(\tilde{t}\,U_b)/h$ at relative positions $x_0'/h = 46.94$ to 3061. Data at CG1' to CG4' are used for validation of the numerical results. Data at $x_0'/h = 1020$, 2041 and 3061 are used within the following analyses and, therefore, plotted in red. (For interpretation of the references to colour in this figure legend, the reader is referred to the web version of this article.)

The size of the moving frames are $T_w = 76\,\text{s}$ and $L_w = 90\,\text{m}$, respectively. These windows are large enough such that both the larger and faster as well as the lower and slower solitons stay within these windows during the whole simulation.

The initial depth and the mean depth under the bore in test No. 20 were $h_0 = 0.098\,\text{m}$ and $h_b = h_0 + \overline{\eta_b} = 0.098\,\text{m} + 0.0196\,\text{m} = 0.1176\,\text{m}$, respectively. The Froude number (9) is thus $\text{Fr}_b = 1.149$ (with $\text{Fr}_{b,\text{nom}} = 1.20$) and U_b follows from Eq. (7) as $U_b = 1.136$ m/s (with $u_0 = 0$). As can be seen in Figs. 7 and 8, the emerging solitons with $A > \eta_b$ propagate faster than U_b and, thus, the moving time frame. In contrast, the backside-solitons with $A < \eta_b$ propagate slower than U_b.

In Figs. 7 and 8, the data are plotted over relative time and position. For clarity of the figures, not all time and space data are plotted here. Nevertheless, all data up to $x_0'/h = 3061$ and $(t_0'\,U_b)/h = 4501$, respectively, are used for the spectral analysis. Selected gauge data that will be discussed in more detail below are plotted in red.

As can be seen in the figures, the free-surface shape of the bore changes continually and significantly as the bore propagates in time and space. Finally, a train of solitons emerges from the initial trapezoidal-shaped bore. Thus, the conventional linear FFT spectra of the different time and space series also are expected to change with time and space.
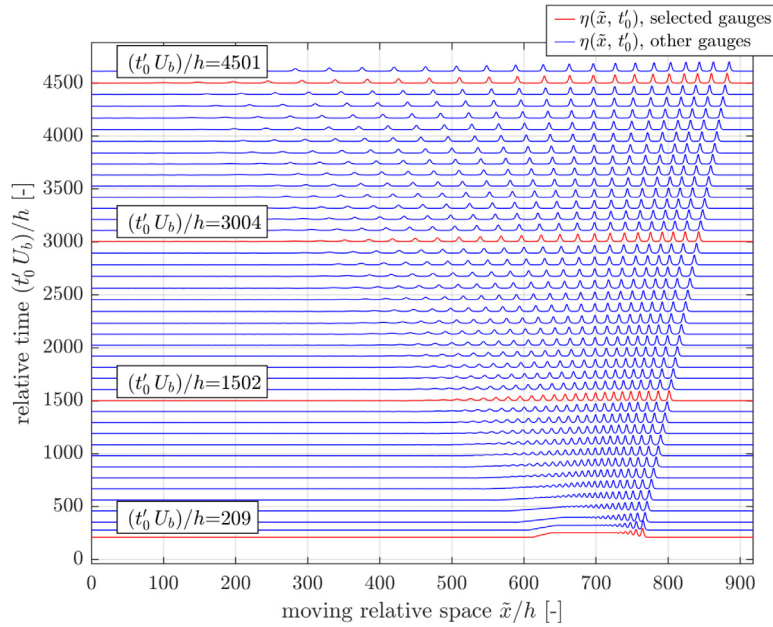
Fig. 8. Spatio-temporal evolution of the free surface space-series $\eta(\tilde{x}, t_0')$ of the initial bore of experiment No. 20 from COULWAVE simulation, plotted over moving relative position $\tilde{x}/h$ at relative timesteps $(t_0' U_b)/h = 209$ to 4640. Data at $(t_0' U_b)/h = 209$, 1502, 3004 and 4501 are used within the following analyses and, therefore, plotted in red. (For interpretation of the references to colour in this figure legend, the reader is referred to the web version of this article.)

The results of the linear FFT are plotted as amplitude–frequency and amplitude–wavenumber spectrograms over relative position and timestep in Figs. 9 and 10, respectively. The FFT amplitudes are given in Figs. 9 and 10a as colour contours for frequencies and wavenumbers in the range $f = [0, 2$ Hz] and $k = [0, 2$ Hz$/U_b]$, respectively. In Figs. 9b–d and 10b–d, the FFT amplitude–frequency and amplitude–wavenumber spectra of the time series at the selected relative positions and timesteps are presented. The according time and space series are highlighted in Figs. 7 and 8 as red lines.

The spectrograms clearly show that the obtained amplitude–frequency spectra are depending on the relative position of the wave gauge or the timestep. These spectra show that, for example, after a relative propagation distance of $x'/h > 500$ suddenly frequency components around $f = 1.25$ Hz appear that then are shifted downwards with increasing propagation distance. The plots also show that for increasing propagation distance the amplitudes of the FFT components with $f < 0.25$ Hz decrease significantly. Thus, in the FFT spectrograms energy is transferred from low-frequency components to higher frequencies as the solitons emerge from the propagating bore. Similar results are obtained for the FFT spectrogram of the space series in Fig. 10. In the latter spectrogram, the maximum low-frequency amplitude does not decrease, but the energy shift is provided by a decreasing width of the low-frequency peak. In general, in the example spectra the number of peaks increases and their frequencies, initially shifted to higher frequencies as the undulations start to develop, now shift to lower frequencies as the bore propagates over a long distance. Therefore, the analysis results confirm the expectation that the linear spectra of the propagating bore are functions of space and time.

The final conclusion is that the conventional linear FFT does not seem to simplify the analysis of the propagation and transformation of the initial bore. The spectral results strongly depend on the position of the wave gauge, and the detection of the higher frequency components and their frequency shifts requires quite large propagation lengths. Furthermore, even if the FFT spectra show frequency shifts, the soliton structure is not evident in the FFT plots.

6. Nonlinear frequency-domain analysis of the bore data using KdV-based nonlinear Fourier transform (KdV-NFT)

Within this section, the numerical data obtained from COULWAVE simulations are analysed using the KdV-based periodic nonlinear Fourier transform (Osborne [10], Brühl [11]) in order to separate the underlying nonlinear cnoidal waves (including discrete solitons) from their nonlinear interactions. First, an example for the nonlinear KdV-NFT spectrum is presented and explained (Section 6.1). Second, the numerical time and space series obtained from COULWAVE simulation of experiment No. 20 are analysed using the periodic KdV-NFT 6.2. Finally, the results of the KdV-NFT analysis of the bore data are summarized 7.4.

6.1. The nonlinear KdV-NFT spectrum

We start the discussion of the nonlinear analysis results with the exemplary KdV-NFT amplitude–frequency spectrum in Fig. 11. This so-called 'nonlinear spectrum' is obtained by applying the periodic KdV-NFT to the numerical COULWAVE
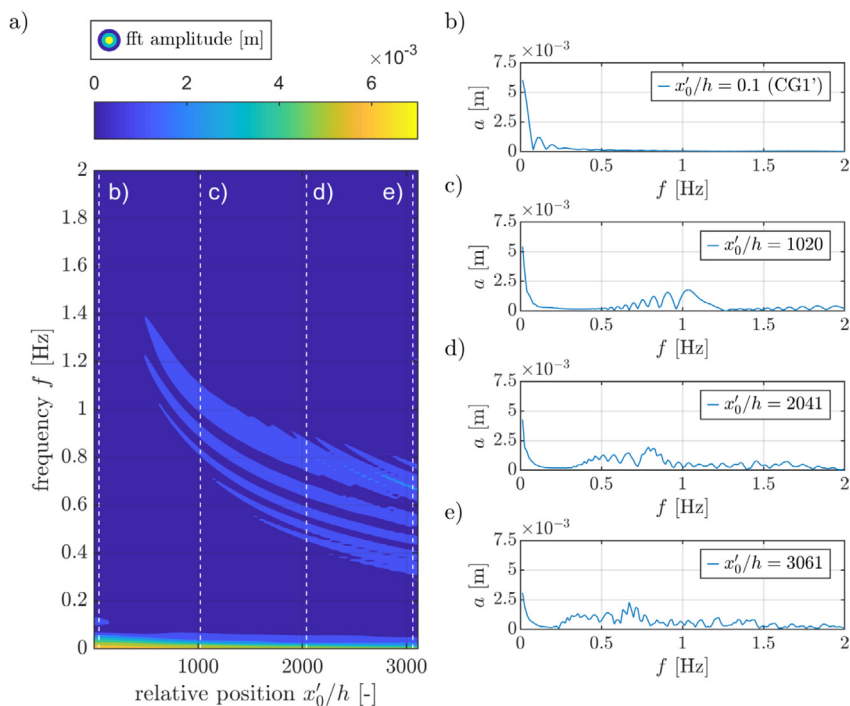
Fig. 9. Amplitude–frequency spectrogram of conventional linear FFT applied to the 206 time series at relative positions x_0'/h from COULWAVE simulations. The FFT amplitudes are given as colour contour in a). For the selected positions $x_0'/h = 0.1$ (CG1'), 1020, 2041 and 3061 (marked with white dashed lines) the amplitude–frequency spectra are also given explicitly in b) to d). (For interpretation of the references to colour in this figure legend, the reader is referred to the web version of this article.)

Fig. 10. Amplitude–wavenumber spectrogram of conventional linear FFT applied to the 850 space series at relative timesteps $(t_0' U_b)/h$ from COULWAVE simulations. The FFT amplitudes are given as colour contour in a). For the selected timesteps $(t_0' U_b)/h = 209$ (first timestep that shows complete initial bore), 1502, 3004 and 4501 (marked with white dashed lines) the amplitude–wavenumber spectra are also given explicitly in b) to d). (For interpretation of the references to colour in this figure legend, the reader is referred to the web version of this article.)
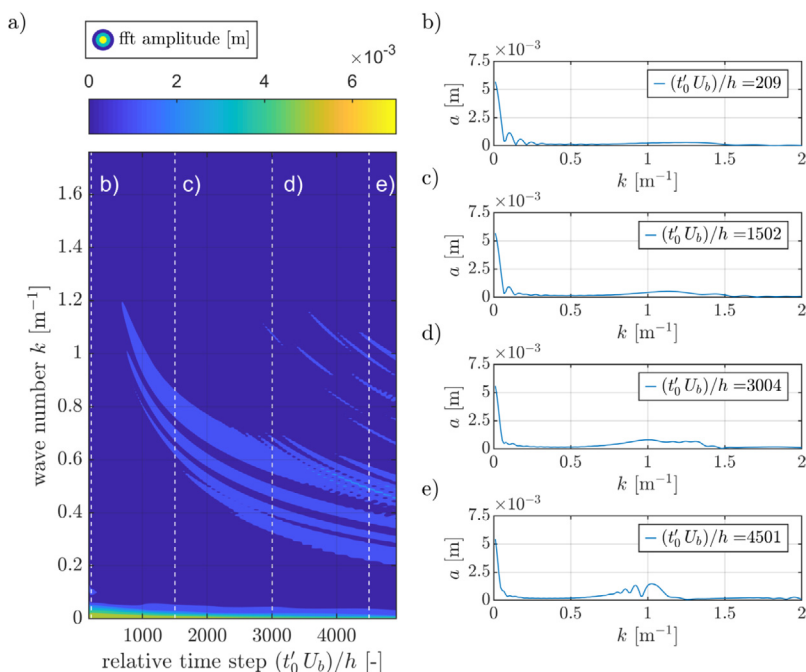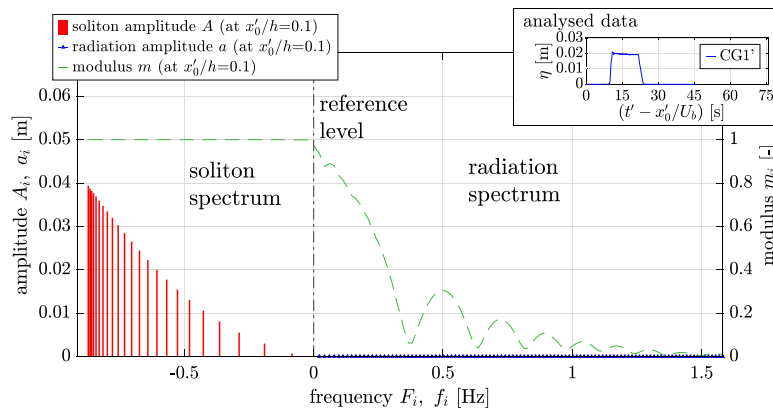
Fig. 11. Periodic KdV-NFT spectrum of the time series at numerical wave gauge CG1' in experiment No. 20 (see upper-right plot within the figure), with the amplitudes A_j of the solitons (red bars), the amplitudes a_k of the oscillatory waves (blue triangles, both on upper left axis), and the moduli m_i (green-dashed curve, upper right axis). (For interpretation of the references to colour in this figure legend, the reader is referred to the web version of this article.)

time-series data $\eta(t')$ obtained at gauge CG1'. The nonlinear spectrum can be read in analogy to the spectra provided by the conventional linear FFT. The wave amplitudes a_k (blue triangles) of the nonlinear spectral radiation components (oscillatory waves) are plotted on the upper left axis as function of the frequencies f_k on the right axis.[8] The main advantage of KdV-NFT is the decomposition of the given data into nonlinear cnoidal waves or hyperelliptic μ-functions instead of linear cosine waves as in FFT. Since the μ-function representation already contains the number and the amplitudes of the determined solitons, we use the parameters obtained from the easier-to-access hyperelliptic functions in the following discussion. Therefore, each combination of frequency (or wavenumber), amplitude and modulus (f_k or k_k, a_k and $m_i < 0.99$ for oscillatory components, and F_j or K_j, A_j and $m_i \geq 0.99$ for solitons (see Brühl [11, Eqs. (3.8) to (3.12)])) represents one hyperelliptic function μ_i from Eq. (6).

In order to clearly distinguish in the plotted spectrum between oscillatory components ('radiation') and solitons, the latter are presented with negative frequencies F_j or wave numbers K_j. This allows to sort the amplitudes within the spectrum according to their height and avoids the overlay of solitons and radiation components. Nevertheless, independent of the negative wavenumber the soliton-like components have only one crest within the analysed time or space window. Every amplitude A_j (red bars) represents one soliton that is identified by the KdV-NFT within the analysed data. Thus, the nonlinear spectrum consists of the soliton spectrum (left part), and the radiation spectrum with the oscillatory waves (right part), see Fig. 11. The reference-level values that separate the two parts are $F_{\text{ref}} = 0$ and $K_{\text{ref}} = 0$. For a given combination of water depth and amplitude, the nonlinearity, and thus the modulus m_i, typically increases with decreasing k_k or f_k. The latter implies that the relative water depth h/L_k decreases with increasing period T_k or wave length L_k. If the relative water depth is sufficiently small, then the determined cnoidal waves are solitons instead of low-frequency oscillatory waves. The reference-level frequency of $f_{\text{ref}} = 0$ Hz in Fig. 11 defines the threshold between oscillatory waves (radiation) and solitons.

The soliton spectrum for gauge CG1' of experiment No. 20 shows the presence of 23 solitons that are plotted as red bars, exactly as expected from the simulation results in Figs. 6–8. The phase spectrum is not presented here, but would be required for the exact reconstruction of the given original data, just as in the inverse FFT. In case of space series $\eta(x)$, the values of a_k, A_j and m_i are obtained for each wave number k_k and K_j, respectively.

Similar to the results for the radiation within this example spectrum, in all analysed time and space series the radiation amplitudes are very small. Thus, we consider the propagating bores to be dominated by the identified solitons. Radiation is of minor importance for the evolution of the free surface. Therefore, in the following discussions of KdV-NFT results we focus on the soliton spectra.

6.2. Nonlinear KdV-NFT analysis of data from numerical simulation

In analogy to the procedure we applied in Section 5, the numerical time and space series are also analysed using periodic KdV-NFT. The resulting nonlinear spectrograms for the soliton spectra are presented in Fig. 12a and Fig. 13a. The soliton amplitudes, A_j, are plotted as colour contour over relative gauge position x_0'/h and relative timestep $(t_0' U_b)/h$. For the relative positions $x_0'/h = 0.1$, 1020, 2041 and 3061 and the relative timesteps $(t_0' U_b)/h = 209$, 1502, 3004 and 4501, respectively, as marked by the dashed lines, the nonlinear spectra are plotted in subfigures b) to d).

---

[8] The radiation amplitudes a_k and the moduli m_i are determined as discrete values for each value within the frequency vector. For better clarity, the moduli are plotted here in line representation without markers.
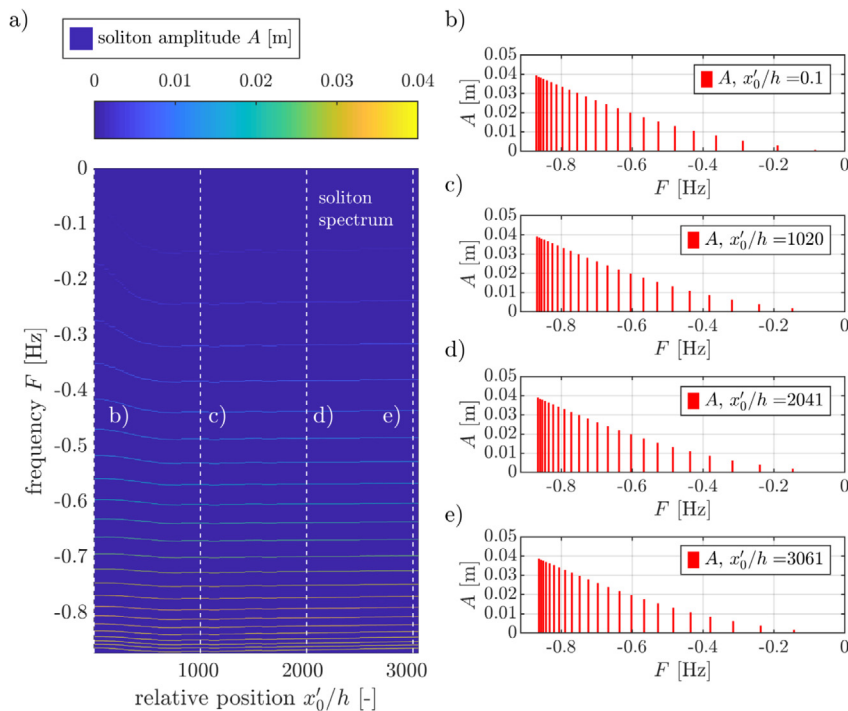
Fig. 12. Nonlinear amplitude–frequency spectrogram of KdV-based periodic time-like nonlinear Fourier transform (tKdV-NFT) applied to the 206 time series at relative positions x'_0/h from COULWAVE simulations. The soliton amplitudes are given as colour contour in a). The radiation spectrum is not presented in the plot. For the selected positions $x'_0/h = 0.01$, 1020, 2041 and 3061 (marked with white dashed lines) the amplitude–frequency spectra are also given explicitly in b) to d). (For interpretation of the references to colour in this figure legend, the reader is referred to the web version of this article.)

The most important difference between the linear FFT spectra in Fig. 9 and the nonlinear KdV-NFT spectra in Fig. 12 is (i) the visibility of discrete solitons in the nonlinear spectra instead of the large low-frequency components in the linear FFT spectra, and (ii) the permanence of the number and amplitudes of the solitons along the spatial and temporal propagation of the bore. The soliton amplitude–frequency spectra do not change significantly over propagation distance. They are independent of the gauge position, but provide reliable results right from the near-field gauges. The nonlinear spectrogram for the space-series analysis in Fig. 13 confirms the results obtained from the time-series analyses. Again, the nonlinear soliton-amplitude spectra remain nearly constant as the bore propagates and develops undulations, and the solitons emerge out of the bore front.

In general, the results of the space-series analyses obtained within this study confirm the results previously obtained from application of KdV-NFT on the time series. This is not self-evident since, as mentioned above, the space-like KdV is only approximately equivalent to the time-like KdV (see Karpman [30, p. 64], Osborne [6, p. 251]).

7. Validation of the KdV-NFT analysis results

In this section, we validate the KdV-NFT results by different approaches: (i) We show that the amplitudes that are determined from time and space series at different positions and timesteps are constant and do not depend on gauge position or simulation timestep and, furthermore, meet the expected values for the maximum amplitude from literature (see Section 7.1). (ii) We show that the soliton amplitudes determined from the nonlinear spectra agree with the far-field peak elevations obtained from time-domain analyses of the simulated data 7.2. (iii) We show that the soliton amplitudes for the four gauges CG1' to CG4' determined with the periodic KdV-NFT as described herein are nearly identical with the amplitudes obtained from an alternative approach, and that the nonlinear superposition of the solitons, including the nonlinear wave–wave interactions, returns the initial data 7.3.

7.1. Stability of the KdV-NFT analysis results in time and space

The expected amplitude A_1 of the leading far-field soliton according to Eq. (15) is twice of the initial bore height η_b. The plot of the bore at CG1 in Fig. 5a shows that the plateau of the bore is not perfectly flat. Thus, for the analyses within this study we decided to calculate the mean bore plateau height for the whole plateau length (here from $t' = 4.725\,\text{s}$ to $t' = 15.590\,\text{s}$) and to set it to the initial bore height, $\eta_b = \overline{\eta_b} = 0.0196\,\text{m}$.
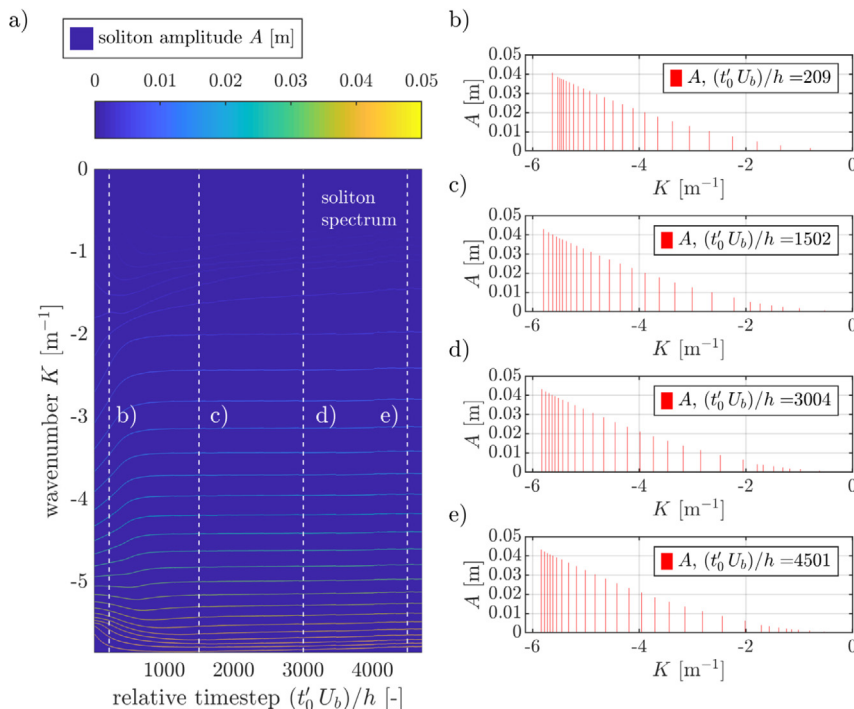
Fig. 13. Nonlinear amplitude–frequency spectrogram of KdV-based periodic space-like nonlinear Fourier transform (sKdV-NFT) applied to 814 space series at relative timesteps $(t'_0 U_b)/h$ from COULWAVE simulations. The soliton amplitudes are given as colour contour in a). The radiation spectrum is not presented in the plot. For the selected timesteps $(t'_0 U_b)/h = 209$ (first timestep that shows complete initial bore), 1502, 3004 and 4501 (marked with white dashed lines) the amplitude–wavenumber spectra are also given explicitly in b) to d). (For interpretation of the references to colour in this figure legend, the reader is referred to the web version of this article.)

Fig. 14 compares the results for the leading amplitudes from time-domain analysis and nonlinear Fourier transform. The maximum elevations $\eta_{max}(x'_0)$ and $\eta_{max}(t'_0)$[9] are plotted as black and blue lines in function of relative position and timestep, respectively. The upper plot in a) shows the dimensional values and the lower plot in b) uses non-dimensional amplitudes, normalized by the (here: mean) bore height η_b. The amplitudes A_1 of the leading solitons as obtained from the KdV-NFT of the time and space series are given as dot-dashed lines.

The initial trapezoidal shape of the bore shows a maximum elevation of $\eta_{b,max} = 0.0209$ m. Thus, the black curve in Fig. 14b, obtained from COULWAVE simulation time series, starts at relative value $\eta_{max}(x'_0)/\eta_b = 1.07$. The blue curve, obtained from COULWAVE simulation space series, starts at $t' = 17.99$ s (relative value $(t'_0 U_b)/h = 209$) after the bore emerged completely out of the left boundary of the generation domain. At this timestep, the maximum elevation is $\eta_{max}(t'_0) = 0.038$ m and the relative elevation is $\eta_{max}(t'_0)/\eta_b = 1.916$. As expected, the time-domain analysis results of the COULWAVE time and space series show the same results. When the bore propagates, the undulations and thus the maximum elevations grow. After about $x'/h = 1000$ the maximum peak elevation is achieved and, starting from here, the values of $\eta_{max}(x'_0)$ and $\eta_{max}(t'_0)$ decrease slightly as the bore propagation continues.

In contrast, the soliton amplitudes $A_1(x'_0)$ (black dash-dotted line) obtained by KdV-NFT analysis[10] of the time series $\eta(x'_0, t')$ already show relative values of around twice of the bore height right from the beginning. This means that even before the undulations have developed and transformed into separate solitons, the far-field soliton is already

---

[9] We denote the absolute maximum of a time series $\eta(x'_0, t')$ measured at a fixed position x'_0 by $\eta_{max}(x'_0)$. Similarly, we denote the absolute maximum of a space series $\eta(x', t'_0)$ measured at a fixed timestep t'_0 by $\eta_{max}(t'_0)$. By $\eta_{max,i}(x'_0)$ we denote the value of the ith largest local maximum in the time series. Similarly, by $\eta_{max,i}(t'_0)$ we denote the value of the ith largest local maximum in the space series. Furthermore, we denote the absolute maximum value of the ith local maximum as obtained from all analysed wave gauges as $\eta_{max,i}(x') = \max(\eta_{max,i}(x'_0))$ for all x'_0, $0 \le x'_0 \le \max(x')$.

[10] We denote the soliton amplitudes calculated by KdV-NFT from a time series $\eta(x'_0, t')$ as $A_i(x'_0)$. Similarly, we denote the soliton amplitudes calculated by KdV-NFT from a space series $\eta(x', t'_0)$ as $A_i(t'_0)$. The i, $1 \le i \le N$, denote the rank-ordered solitons with $A_1(x'_0)$, $i = 1$, representing the largest, leading soliton obtained from a numerical time series at gauge position x'_0.
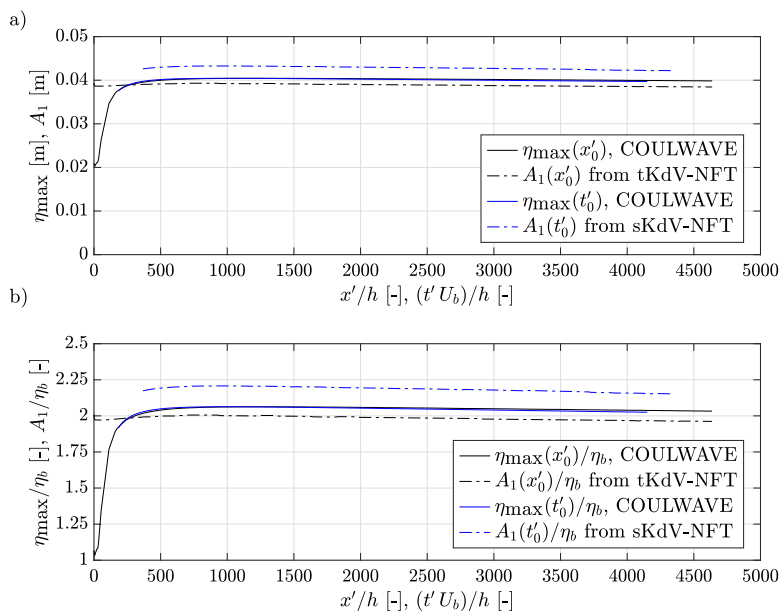
Fig. 14. Comparison of maximum peak elevations $\eta_{max}(x'_0)$ and $\eta_{max}(t'_0)$ from COULWAVE wave gauge time series $\eta(x_0, t')$ and space series $\eta(x', t'_0)$ and leading solitons $A_1(x'_0)$ and $A_1(t'_0)$ from KdV-NFT analysis of the time and space series, respectively. a) Dimensional elevations and amplitudes as function of the relative position x'/h and relative time $(t' U_b)/h$. b) Relative elevations η_{max}/η_b and relative amplitudes A_1/η_b as function of relative position and relative time. (For interpretation of the references to colour in this figure legend, the reader is referred to the web version of this article.)

identified within the KdV-NFT from the initial bore and the near-field data. Nevertheless, the expected relative values of $A_1(x'_0)/\eta_b = 2$ from Eq. (15) are met (see Fig. 14b), but the maximum peak elevation as observed in the numerical simulation data is underestimated by about 3%.

The nonlinear analyses of the space series $\eta(x', t'_0)$ also provide quite constant values for $A_1(t'_0)$ and, therefore, $A_1(t'_0)/\eta_b$, but here the spectral results overestimate the simulated soliton amplitude by about 10%. Anyway, based on the existing results we can clearly present and discuss the methodology, the results and the interpretation of the application of KdV-NFT on propagating bores.

In Hammack and Segur [5], a comparison is given of experimental observations of emerging solitons with analytical results for these data obtained from the KdV equation. Since they used a vertical piston for the generation of the waves and generated different wave types, they did not analyse long bores as within this study. Furthermore, their flume was too short to allow complete separation of the emerging solitons. They also pointed out that the viscosity affected the experimental results. Since the KdV does not include viscous effects, we must be careful with quantitative comparisons of the respective results. Furthermore, they used the space-like KdV from Eq. (1) for the calculation of the theoretical values of $A_1(t'_0)$ and compared these results with the observations for $A_1(x'_0)$ from experimental time series. They found the deviations between observed and calculated values to be between 2% and 21% (Hammack and Segur [5, Tab. 1]). Based on equations by Keulegan [55, Eqs. (44), (45)], they estimate the effect of viscous dissipation to be responsible for about 12% of the amplitude decay of the solitons if $A_1/h \leq 0.5$. In our example case $A_1/h \approx 0.4$, but bottom friction is not activated in the numerical simulation. But a wave breaking model is used that might introduce some eddy viscosity in the numerical simulation, leading to lower dissipation than expected from explicit consideration of bottom friction. Nevertheless, the deviations observed within the present study (3% and 10%) are within the range observed by Hammack and Segur [5],

According to Osborne [6, p. 251], the different dispersion relations that apply to the space-like and the time-like KdV cause a physical difference between the two forms of the KdV equation. Therefore, different spectral results are to be expected when applying both sKdV and tKdV to the space-series and time-series data, respectively, from the same simulation. Furthermore, Osborne [6, p. 251] states that 'in this context it is unclear whether one form of KdV is preferred over the other'. The results in Fig. 14 show that for the one experiment analysed in the present study, the results of tKdV are closer to the maximum soliton amplitudes observed in the simulations. Nevertheless, they underestimate the numerical values by about 3%. In contrast, the results of the sKdV overestimate the numerical results by about 10%.

In Fig. 15, we quantitatively compare the soliton amplitudes obtained by the tKdV-NFT from the time series at all gauges. The initial results are based on wave-gauge recordings, and the results of the space-series analysis requires further investigations. Therefore, the following analyses are applied to the time-series data. For each of the 23 largest solitons
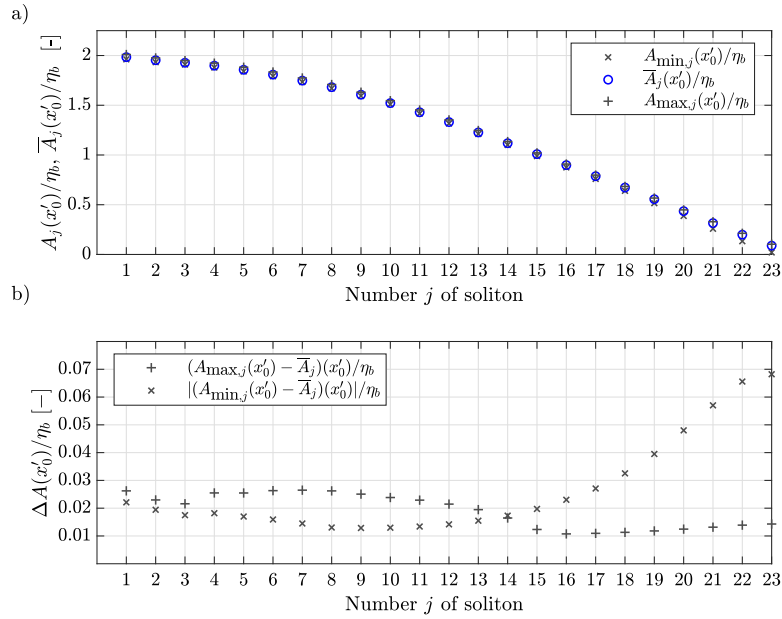
Fig. 15. Comparison of the tKdV-NFT results from the different 206 time series of experiment No. 20: a) Relative values of mean amplitude $\overline{A}_j(x'_0)/\eta_b$, minimum and maximum amplitudes $A_{\min,j}(x'_0)$ and $A_{\max,j}(x'_0)$ for each of the largest 23 solitons, $1 \leq j \leq 23$, calculated at the 206 gauge positions. b) Deviations between mean and minimum value and between mean and maximum value for each soliton.

($j = 1, \ldots, 23$),[11] we used the results from all 206 gauges to calculate the mean value $\overline{A}_j(x'_0)$ (blue circles in Fig. 15a, the maximum and the minimum amplitudes, $A_{\max,j}(x'_0)$ (black '+') and $A_{\min,j}(x'_0)$ (black 'x'). All values are given as relative values with respect to η_b. The plot in Fig. 15b shows the relative deviations $(A_{\max,j}(x'_0) - \overline{A}_j(x'_0))/\eta_b$ and $|(A_{\min,j}(x'_0) - \overline{A}_j(x'_0))|/\eta_b$. The results show that for the larger solitons 1 to 17 the determined amplitudes vary less than 3% from the mean values. For solitons 18 to 23 the maximum values are about 1% to 1.5% above mean, whereas the minimum value shows larger deviations up to 7% for soliton 23. Nevertheless, in this example the maximum amplitudes vary between 1.1% and 2.6% from the mean, and the minimum values for solitons 1 to 17 differ between 1.3% and 2.7% from the mean amplitude. The amplitudes of the leading solitons with amplitudes larger than the initial bore height, $A_1(x'_0) \leq \eta_b$, are determined within 5% deviation from the observed far-field amplitude.

7.2. Comparison of simulation data and KdV-NFT analysis results

In order to visualize the development of the peak elevations from the initial bore over an undulating bore up to the discrete far-field solitons, Fig. 16 shows the evolution of the 23 relative peak elevations $\eta_{\max,i}(x'_0)/\eta_b$ obtained from the COULWAVE time series as a function of the 206 relative wave-gauge positions x'_0/h from near to far field up to relative position $x'_0/h = 400\,\text{m}/0.098\,\text{m} = 4082$. Here, $\eta_{\max,i}(x'_0)$ is the peak elevation of the ith undulation (local maximum) or soliton that has already evolved from the bore, x'_0 its position in the numerical domain, $h = 0.098\,\text{m}$ the water depth, and $\eta_b = \overline{\eta_b} = 0.0196\,\text{m}$ the (mean) plateau elevation of the incident bore at the gauge CG1' at $x'_0 = 0.01\,\text{m}$. The expected far-field amplitude of the leading soliton according to Eq. (15) with $\eta_{01,\exp} \approx 2\,\eta_b = 0.0392\,\text{m}$ is plotted in Fig. 16 as red-dashed line at the relative value $\eta_{01,\exp}/\eta_b = 2.0$. The elevations of the 23 largest peaks are plotted as coloured graphs from top to bottom, starting with the first undulation and leading soliton 01 at the top and ending with peak 23 at the bottom. The graphs are labelled with the number $[i]$ of the respective peak. The larger peaks are identified within the propagating bore very soon, whereas the lower peaks need certain distances to separate from the back of the bore. Thus, their graphs start at larger propagation distances. The peak values at positions $x'_0 = 100\,\text{m}$, 200 m and 300 m can be found in the numerical gauge data in Fig. 6. For comparison, the positions of the near-field gauges CG2' to CG4' from Fig. 5 (at about $x'_0 = 47\,h$, $97\,h$ and $137\,h$) and the far-field gauge locations from Fig. 6 are indicated as vertical grey dash-dotted

---

[11] In the periodic tKdV-NFT analysis a total of 24 to 32 solitons have been determined, depending on the gauge position. The amplitudes $A_{24}(x'_0)$ obtained from the different gauge data show values in the range $A_{24}(x'_0) = 0.000018\,\text{m}$ to $0.000412\,\text{m}$. The amplitudes $A_{32}(x'_0)$ lie in the range $A_{32}(x'_0) = 0.000068\,\text{m}$ to $0.000076\,\text{m}$. For comparison: the amplitudes $A_{23}(x'_0)$ have values in the range $A_{23}(x'_0) = 0.000401\,\text{m}$ to $0.002017\,\text{m}$. Due to the small values and for better comparison with the observation of the simulation results in Fig. 6, in the following discussion we limit the number of solitons to $N_{\text{sol}} = 23$.
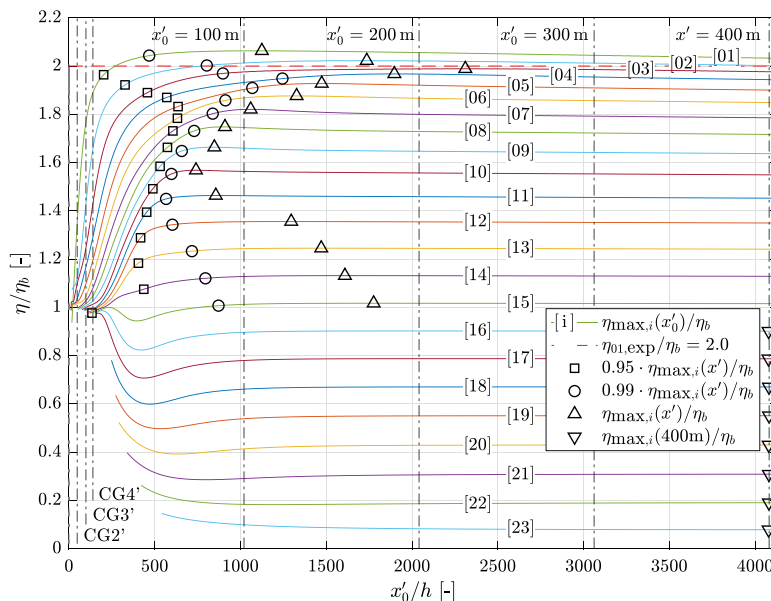
Fig. 16. Evolution of the relative elevations $\eta_{\max,i}(x_0')/\eta_b$ over relative position x'/h, with $\eta_{\max,i}(x_0')$ the value of the ith largest local maximum in the time series. The expected amplitude of the leading soliton according to Eq. (15) is plotted as red-dashed line at $\eta_{01,\exp}/\eta_b = 2$. For the solitons with maximum relative amplitudes $\eta_{\max,i}(x')/\eta_b > 1$ the maximum relative peak elevations are marked with '△'. The positions where 95% and 99% of the maximum values are reached are denoted with 'x' and 'o', respectively. For the peaks with maximum elevation lower than the initial bore height, the elevations obtained at $x_0' = 400$ m ($x_0'/h = 4082$) marked by '▽'. For comparison, the relative positions of the gauges CG2' to CG4' (see Fig. 5) and gauge positions $x_0' = 100$ m, 200 m, 300 m and 400 m (see Fig. 6) are given by vertical dash-dotted lines. (For interpretation of the references to colour in this figure legend, the reader is referred to the web version of this article.)

lines in the figure. Furthermore, in addition to the space-series results in the coloured graphs the figure also shows the soliton amplitudes as determined by periodic tKdV-NFT as grey-dashed lines from top (leading soliton 01) to bottom (lowest soliton 23). The results show that for the larger solitons the periodic tKdV-NFT underestimates the amplitudes compared to the time-domain analysis of the simulation data. This is in agreement with the results presented in Fig. 14. For the lower solitons, the KdV-NFT results fit better with the observed peak elevations. We give a more detailed view on and a description of the nonlinear results later below in Fig. 17.

The plot of the peak development in Fig. 16 shows that the leading soliton 01 (topmost green curve) evolves out of the bore front quite fast and reaches its relative maximum value $\eta_{\max,01}(x')/\eta_b = 2.063$ (black upward-pointing triangle) after about 1125 times the water depth. But after a propagation length of about 200 and 470 times the relative water depth, 95% (black square) and 99% (black circle), respectively, of the maximum relative elevation are already reached. In the plot, the values for the 95%, 99% and the maximum elevations are marked for all solitons 01 to 15, which have maximum amplitudes above the initial bore height, $\eta_{\max,i}(x') > \eta_b$. After having reached the maximum peak elevation, the elevations of these solitons slightly decrease as they propagate further downwave. Since the evolution of the amplitudes around the maximum values is nearly horizontal, numerical noise, friction or other effects might significantly affect the determined position of the maximum peak elevation. Therefore, we consider the 99% values to be more robust and will use these values for further discussion. For solitons 16 to 23, the evolution plot shows peak amplitudes smaller than the initial bore height, $\eta_{\max,i}(x') < \eta_b$. Some of these elevation graphs show local minima before they increase again and reach their far-field amplitudes. Therefore, for further proceeding we consider the final elevations $\eta_{\max,i}(x_0' = 400$ m$)$ (black downward-pointing triangles) as observed at relative position $x_0'/h = 4082$. The detailed values for all solitons are given in Tables 3 and 4.

In general, the time-domain results of the numerical simulation data in Fig. 16 confirm Eq. (15) whereupon the expected amplitude of the leading soliton is $\eta_{01,\exp} \approx 2\,\eta_b$. In the selected simulation, we obtain a maximum factor of $\eta_{\max,01}(x')/\eta_b = 2.063$, which is slightly above the expected value. Note that due to the uneven plateau height of the initial bore alternative approaches might be chosen for the calculation of the bore height that would lead to different results for the relative soliton amplitudes. In this example, using the maximum bore height, instead of the mean value, would provide a value of $\eta_{\max,01}(x')/\eta_{b,\max} = 0.0404$ m$/0.0209$ m$= 1.935$. With increasing downstream position, the maximum bore elevation is increasing due to the emerging first undulation, and the quotient of final and current bore height is decreasing further until the leading soliton has emerged and the quotient reduces to 1 (in accordance with Eq. (14)). Therefore, twice the bore height only gives a good estimate of the leading far-field soliton amplitude in the early stages when the plateau is still horizontal and the undulations have not yet developed.

Table 3

Maximum absolute and relative peak elevations $\eta_{\max,i}(x')$ and $\eta_{\max,i}(x')/\eta_b$ and their relative positions $x'_{\max,i}/h$, $x'_{95\%,i}/h$ and $x'_{99\%,i}/h$ were the maximum value, 95% and 99% of the maximum elevation, respectively, are reached for solitons with maximum elevations $\eta_{\max,i}(x') \geq \eta_b$. All data are obtained from the COULWAVE time series. Furthermore, the absolute and relative soliton amplitudes A_j(CG2') and A_j(CG2')η_b from periodic KdV-NFT of the time series at gauge CG2' are listed.

elevation i / soliton j	$\eta_{\max,i}(x')$ [m]	$\eta_{\max,i}(x')/\eta_b$ [−]	$x'_{i,\max}/h$ [−]	$x'_{i,95\%}/h$ [−]	$x'_{i,99\%}/h$ [−]	A_j(CG2') [m]	A_j(CG2')/η_b [−]
01	0.0404	2.063	1124	202	468	0.0386	1.971
02	0.0396	2.022	1736	327	804	0.0380	1.939
03	0.0390	1.988	2311	457	898	0.0375	1.913
04	0.0386	1.968	1897	570	1244	0.0369	1.884
05	0.0378	1.928	1473	636	1069	0.0361	1.843
06	0.0368	1.876	1327	632	912	0.0352	1.795
07	0.0357	1.821	1059	606	838	0.0340	1.735
08	0.0343	1.748	910	574	730	0.0327	1.669
09	0.0326	1.664	848	531	658	0.0312	1.593
10	0.0307	1.568	740	489	597	0.0296	1.509
11	0.0287	1.463	856	453	566	0.0278	1.416
12	0.0266	1.356	1296	418	603	0.0258	1.317
13	0.0244	1.245	1471	405	717	0.0237	1.211
14	0.0221	1.131	1609	436	795	0.0216	1.101
15	0.0199	0.986	1776	134	872	0.0194	0.989

Table 4

Absolute and relative final elevations $\eta_{\max,i}(x'_0 = 400\,\mathrm{m})$ and $\eta_{\max,i}(x'_0 = 400\,\mathrm{m})/\eta_b$ at relative position $x'_0/h = 4082$ '$(x'_0 = 400\,\mathrm{m})$ for solitons with maximum elevation $\eta_{\max,i}(x') < \eta_b$. The data are obtained from the COULWAVE time series. Furthermore, the absolute and relative soliton amplitudes A_j(CG2') and A_j(CG2')/η_b from periodic KdV-NFT of the time series at gauge CG2' are listed.

elevation i / soliton j	$\eta_{\max,i}(x'_0)$, $x'_0 = 400\,\mathrm{m}$ [m]	$\eta_{\max,i}(x'_0)/\eta_b$, $x'_0 = 400\,\mathrm{m}$ [−]	A_j(CG2') [m]	A_j(CG2')/η_b [−]
16	0.0177	0.901	0.0172	0.875
17	0.0154	0.787	0.0149	0.760
18	0.0131	0.670	0.0125	0.640
19	0.0108	0.551	0.0101	0.515
20	0.0084	0.429	0.0076	0.338
21	0.0060	0.308	0.0051	0.260
22	0.0037	0.190	0.0004	0.022
23	0.0015	0.078	0.00002	0.001

Furthermore, the results show that in this example case the leading soliton amplitude increases quite fast and reaches 95% of the final peak elevation after a propagation length of about 200 times the water depth or $\Delta x' = 20\,\mathrm{m}$, and 99% maximum peak elevation after about $x' = 470\,h$ or $\Delta x' = 46\,\mathrm{m}$. After that, the peak amplitude reaches its maximum at relative position 1124 which means the propagation of $\Delta x' = 110\,\mathrm{m}$ in a water depth of 0.098 m. Finally, the amplitude shows a slight decrease while the soliton propagates further downstream. Disregarding the slight decrease, this is the expected behaviour of a soliton that evolves completely out of the propagating bore front and then propagates as stable wave form with double bore height and without changes in shape. The same applies accordingly to the succeeding solitons that show lower amplitudes and need longer propagation lengths to fully develop, as can be seen in Fig. 16 and Tables 3 and 4.

In addition to the time-domain analysis results discussed above, in Tables 3 and 4 we also present the absolute and relative soliton amplitudes A_j(CG2') and A_j(CG2')/η_b obtained by periodic KdV-NFT on the time series from near-field gauge CG2'. The comparison of the results for the maximum elevations and the KdV-NFT results shows that the maximum elevations are predicted by the periodic KdV-NFT up to 5% precision for the solitons 01 to 18. Note that within the numerical simulation relative propagation distances between 740 and 2311 times the water depth are required to reach the maximum elevations. In contrast, by application of the periodic KdV-NFT the future elevations of the propagating bore can be predicted from the near-field data at $x'_0/h = 48$.
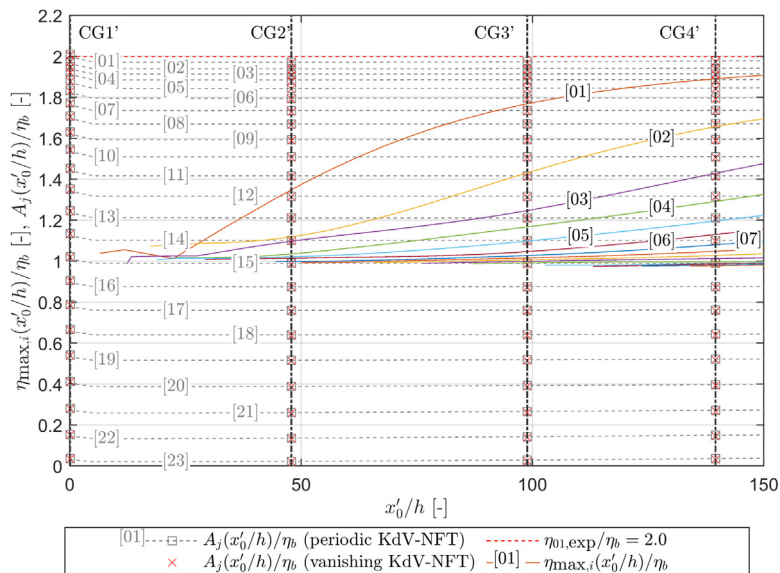
Fig. 17. Detail of the evolution of the relative elevations $\eta_i/\eta_{b,\max}$ over relative position x'_0/h during the propagation of the initial bore-shaped wave, with η_i the peak elevation of the ith undulation or soliton. The expected amplitude of the leading soliton of $2\,\eta_{01,\max}/\eta_{b,\max}$ according to Eq. (15) is plotted as red-dashed line. (For interpretation of the references to colour in this figure legend, the reader is referred to the web version of this article.)

7.3. Reconstruction of the free surface by nonlinear superposition of the identified solitons

The bores that we analyse here are not periodic oscillations but localized wave packages. Therefore, we can also use KdV-NFT algorithms that are developed for vanishing boundary conditions[12] for the analysis. Similarly to periodic KdV-NFT, the vanishing KdV-NFT is also able to extract solitons from shallow-water data, with the number and the amplitudes of the solitons depending on the relative water depth. In this section, we will use results obtained from the vanishing KdV-NFT to verify the above results from the periodic KdV-NFT. We will furthermore use the 'nonlinear superposition' for the vanishing case to illustrate how the individual solitons from the nonlinear decomposition step-by-step add up to the original bore. The nonlinear superposition requires the phase information of the solitons that have not been necessary for the previous discussions related to the soliton numbers and amplitudes. The calculation of the soliton phases, which is not trivial from a numerical point of view, is provided by the algorithm by Prins and Wahls [46]. For the nonlinear superposition of the large number of solitons, which is also not trivial from a numerical point of view, we will use the algorithm in Prins and Wahls [52] to generate the signals corresponding to the N_{sol} largest solitons, for increasing values of N_{sol}.

In Fig. 17, we show a zoomed in portion of Fig. 16 including the relative soliton amplitudes $A_j(x'_0/h)/\eta_b$ as obtained by the vanishing KdV-NFT (red crosses). Furthermore, we extended the grey-dashed lines of the periodic KdV-NFT results with the discrete data at the gauges CG'1 to CG'4 (grey squares). The results for these data (see Fig. 5) clearly show that both results, although obtained for different boundary conditions, provide the same spectral decomposition at the four near-field gauges. The results in Fig. 17 verify that the periodic KdV-NFT provides the same results as the vanishing KdV-NFT for the exemplary bore data. Therefore, the periodic KdV-NFT algorithm presented within this study can be assumed to provide reliable results for the analysis of the propagating bore. This confirms the results in Osborne [6] who successfully applied the periodic NFT for the analysis of localized wave data.

In the next step, we show that the application of the algorithm in Prins and Wahls [52] for the nonlinear superposition of the $N_{\text{sol}} = 23$ solitons returns the initial bore signal at gauge CG1' (see Figs. 18, 19). From the phase information that is returned by the vanishing KdV-NFT, we can predict the phase offsets Φ_j of the separated solitons in the far field (see Eq. (13)), Prins and Wahls [46]. These are listed in Table 5. More generally, the inverse KdV-NFT algorithm transforms the spectrum into a time signal that includes the nonlinear interactions. For visualization of the significant influence of the nonlinear interactions within the bore, Fig. 18 shows the stepwise nonlinear superposition of the first twelve solitons for the vanishing case. In the upper left plot, for $j = 1$, the largest soliton is plotted as red-dashed line. For each soliton, the so-called norming constant (see Prins and Wahls [46]) has the same magnitude in every plot in Figs. 18 and 19 in which

---

[12] For a signal with *vanishing* boundary condition, the elevations vanish at infinity (sufficiently fast). Thus, for vanishing space series applies $\lim_{x \to -\infty} \eta(x, t_0) = \lim_{x \to +\infty} \eta(x, t_0) = 0$. Similarly, for vanishing time series applies $\lim_{t \to -\infty} \eta(x_0, t) = \lim_{t \to +\infty} \eta(x_0, t) = 0$.

Table 5
Spectral parameters of the data at CG1': For each of the 23 solitons the amplitude A_j and the phase Φ_j with respect to t' and $x_0' = 0.01\,\text{m}$ of the discrete emerged far-field soliton are given.

Soliton j	A_j [m]	Φ_j [−]
01	0.0394	26.61
02	0.0387	31.97
03	0.0382	36.90
04	0.0377	41.06
05	0.0369	44.00
06	0.0359	46.51
07	0.0347	48.28
08	0.0334	49.88
09	0.0319	50.88
10	0.0302	51.53
11	0.0284	51.75
12	0.0265	51.66
13	0.0244	51.20
14	0.0221	50.40
15	0.0200	49.35
16	0.0177	47.98
17	0.0154	46.28
18	0.0130	44.03
19	0.0106	41.03
20	0.0080	37.08
21	0.0055	31.88
22	0.0030	24.81
23	0.0007	13.30

that solitons appears. This determines the positions of each of the waves in Figs. 18 and 19. For comparison, the initial bore data is also plotted (black-dashed curve).

Since only one soliton is added in the case j=1, no wave–wave interactions occur and the nonlinear superposition (blue curve) is identical with this first soliton. The red dashed line in the plot for j=2 shows the soliton that is nonlinearly superposed with the previous soliton (blue line for j=1). The blue line in the plot for j=2 shows the time series corresponding to a spectrum that consists of the amplitude and phase information of the tallest two solitons. With increasing number of added solitons, we see that the time series that correspond to the partial spectra show a number of crests that equals the number of solitons in the spectrum. Note that the elevations of these crests clearly differ from the amplitudes of the superposed solitons. Furthermore, when we include the lower solitons, the troughs do not return to zero anymore and the peaks become flatter. Obviously, these results are significantly different from a simple linear superposition of the individual solitons.

The lower-right plot in Fig. 18 shows the inverse KdV-NFT of the twelve largest solitons from the nonlinear spectrum. The result is a long undulating bore with smaller maximum elevation than the largest soliton. The data show that the transformation from the single solitons to the desired bore shape has started, but is still far from being complete since not all solitons have been added yet. Thus, the remaining eleven solitons with $13 \leq j \leq 23$ are added one by one in the plots in Fig. 19. As can be seen in Eq. (12) and especially in Fig. 19, the width of a soliton increases as its amplitudes decreases. As a consequence, the inclusion of the lower-amplitude solitons in the spectrum has an effect over the whole bore width. Furthermore, the results clearly show that all 23 solitons are required to return the initial signal. Especially the inclusion of the two smallest solitons significantly reduces the remaining ripples in the nonlinear superposition. After all 23 solitons have been included in the reconstructed spectrum, small differences to the original signal remain. These differences occur because the radiation part of the nonlinear spectrum was not considered in the reconstruction.

Finally, the nonlinear superposition of only the solitons including their interactions returns the initial signal with good accuracy. This confirms that the bore data indeed are soliton-dominated. The remaining variations are, as already mentioned above, due to the absence of the radiation components. The addition of the rank-ordered solitons causes phase shifts and widens the bore while preserving an approximately symmetric shape of the nonlinear superposition. These effects, and especially the reduction of the peak elevations by the newly added solitons from $A_1 = 2\eta_b$ in the case $j = 1$ down to η_b for $j = 23$ cannot be explained by simple linear superposition.

7.4. Conclusion of KdV-NFT analysis results

The nonlinear spectra obtained from the time- and space-series analyses clearly prove that the evolution of the initial trapezoidal-shaped bore (see Fig. 5a) into a train of 23 solitons (see Fig. 6c) can already be predicted from the measurement at the first gauge CG1. The constant colours of the soliton amplitudes in Figs. 12 and 13 and the more detailed analyses in Section 7.1 show that after some initial changes, the number and the respective amplitudes of the emerging solitons in the nonlinear spectra are approximately constant in time and space. The changes in the soliton frequencies that are observed
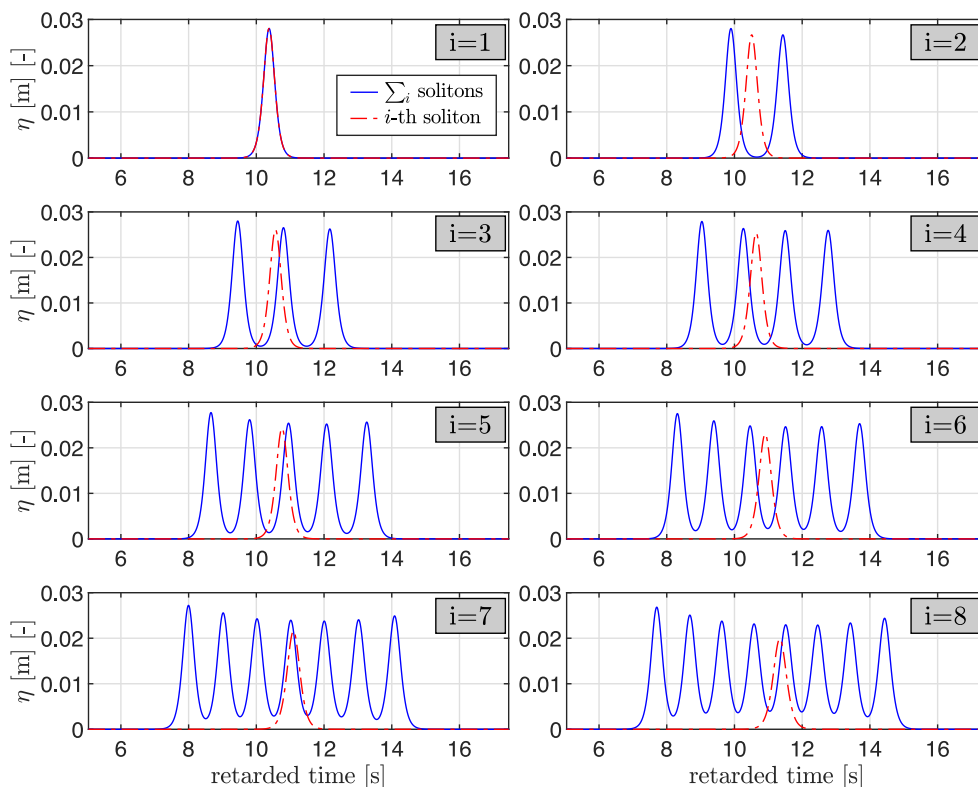
Fig. 18. The inverse KdV-NFT of a stepwise completed spectrum for the data at CG1' (part 1): The solitons are added one by one to the spectrum in order of amplitude, starting from the tallest ($j = 1$). The blue lines show the inverse KdV-NFT of the first twelve of these spectra. Those of the remaining spectra are presented in Fig. 19. (For interpretation of the references to colour in this figure legend, the reader is referred to the web version of this article.)

in the near field (up to $x'/h \approx 500$, $(t' U_b)/h \approx 500$) are due to the evolution of the emerging solitons. According to Eqs. (10) and (12), the wavenumbers and frequencies of the solitons are a function of their amplitudes. Thus, increasing amplitudes lead to increasing (absolute) wave numbers and frequencies. Decreasing amplitudes compared th the initial bore height lead to decreasing (absolute) values. Once the solitons have reached their final amplitudes, their wavenumbers and frequencies remain constant. Harmonic generation, as observed in the FFT spectrograms (Figs. 9 and 10), cannot occur in the periodic or vanishing KdV-NFT (Figs. 12 and 13) as long as the waves propagate in constant depth. Hence, the amplitudes in the KdV-NFT spectrum are independent of the gauge position or the selected timestep. Thus, the KdV-NFT reliably reveals the inner nonlinear soliton structure of the propagating bore and allows to predict the far-field solitons already from near-field bore data.

8. Summary

In this study, the periodic KdV-based nonlinear Fourier transform (KdV-NFT) was used to analyse the propagation of an undular bore in constant depth over long distances. First, the basics of the periodic KdV-NFT, the theoretical background of bore generation in flumes, the classification of bore waves, and the relation of solitary waves to the KdV equation were briefly given. Then, the experimental set-up and the programme were described that provided the experimental data basis for the analyses in this study. Due to the limited length of the experimental flume, we conducted numerical simulations with COULWAVE in order to significantly extend the bore propagation distance up to relative length $x'/h = 3061$ and relative time $(t' U_b)/h = 4501$ (according to dimensional values $x' = 300$ m and $t' = 388.3$ s, respectively). We validated the numerical results with the data from the flume experiments.

The selected propagation distance is much larger than in previous studies and, thus, allows the complete emergence of all far-field solitons from the initial trapezoidal-shaped bore. Therefore for the first time, comparative analyses using both time-like and space-like periodic KdV-NFT could be performed for the whole propagation process from the initial bore to the far-field train of solitons. For the exemplary case selected in this study, the simulations show the development of 23 solitons in the far field, with the amplitude of the leading soliton being, as expected, about twice of the initial bore height.
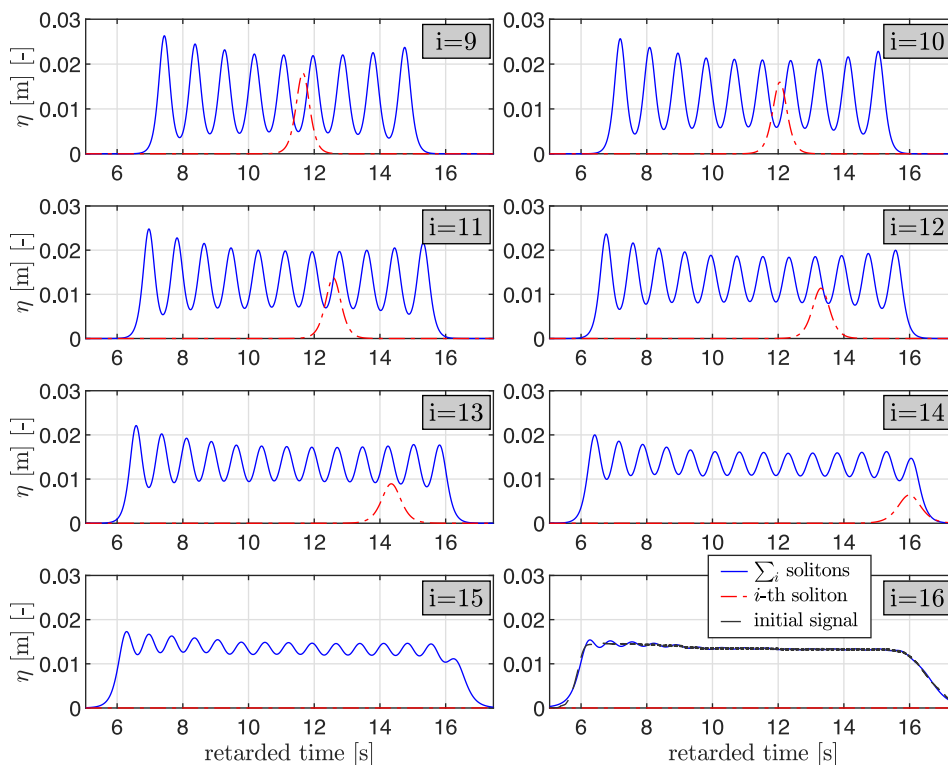
Fig. 19. The inverse KdV-NFT of a stepwise completed spectrum for the data at CG1' (part 2): The solitons are added one by one to the spectrum in order of amplitude, starting from the tallest ($j = 1$). The inverse KdV-NFT of the first twelve spectra is presented in Fig. 18. The blue lines here show those of the remaining spectra. (For interpretation of the references to colour in this figure legend, the reader is referred to the web version of this article.)

We started the analyses of the numerical data with the conventional linear fast Fourier transform (FFT). The results show, as expected, that the linear FFT fails to capture the solitons forming the initial bore and its fission. The spectral results strongly depend on the position of the wave gauge. The FFT spectra of the propagating bore are not invariant but functions of the gauge position. The soliton structure of the bore is not evident in the FFT plots, neither in the far-field results nor in the near-field analysis.

The nonlinear analyses with the periodic KdV-NFT started with the introduction of the nonlinear spectrum as a graphical representation of the results of the analysis. The nonlinear spectrum shows the amplitudes A of the identified solitons as discrete values, and contains the modulus m of the hyperelliptic functions as a measure for the nonlinear character of each spectral component in the spectrum. The KdV-NFT spectrum of the bore is dominated by solitons and matches the number of solitons and the soliton amplitudes that are obtained by visual inspection of the far-field data. The nonlinear analysis of the time series at different locations shows that – in contrast to the FFT results – the amplitudes of the nonlinear spectra obtained by KdV-NFT are (nearly) invariant to the gauge position even though the propagation of the bore is only approximated by the KdV. Since the nonlinear amplitude spectrum is invariant, the soliton structure including number and amplitudes of the far-field solitons can be predicted based on one single wave gauge measurement anywhere in the propagation path of the undular bore, including the near-field gauge data. Thus, the observed free surface of the initial trapezoidal-shaped bore, the undulated bore as well as the discrete solitons in the far field are modelled by the same nonlinear spectral components. The completely different free-surface elevations are caused primarily by the nonlinear interactions between the basic components that initially overlap and are later separated in the far field.

The analyses of the space series with the space-like KdV-NFT confirm the results obtained from the time series analysis. Also here the nonlinear amplitude spectra are almost invariant in time and the far-field solitons can be predicted from any timestep of the bore propagation. Nevertheless, the analysis of time series underestimates the observed maximum soliton amplitude by about 5% whereas the analysis of the space series overestimates the maximum solitons amplitude by about 7%. Based on the exemplary analysis of one single experiment within this study, no final conclusion can be drawn if this applies in general. Further investigations with a larger number of bores will be performed in order to answer this question.

We determined the evolution of the peaks of the undular bore and the solitons from the simulation space series. The results show that the leading soliton in the considered case requires relative propagation lengths of about 200 and 470

times the water depth to reach 95% and 99% of its maximum amplitude, respectively. For all solitons within the considered case, the 95% amplitudes are reached between about 135 and 635 times the water depth, the 99% amplitudes are observed between about 470 and 1245 times the water depth. These latter results could only be obtained by the investigation of much longer time series than in the current literature.

As final evidence that the initial trapezoidal-shaped bore in fact can be generated by nonlinearly interacting solitons, we showed how the free surface looks for a series of partial spectra. The obtained results impressively show how the characteristic shapes of the individual solitons slowly disappear as more and more solitons are added to the spectrum. Finally, the initial trapezoidal shape reappears. This is another evidence that the solitons do not appear out of the blue or are 'generated' as the bore propagates. The dispersion effects due to the different celerities of the solitons with different amplitude cause the solitons to emerge rank-ordered out of the bore front in the far field.

In conclusion, we have demonstrated for the first time that the KdV-NFT is able to reliably predict the hidden solitons within non-breaking undulating bores in constant depth from both time and space series, respectively, even when very long propagation distances and durations are required. Predictions from initial near-field time series thereby proved to be slightly more accurate than predictions based on initial near-field space series. Finally, we can conclude that the periodic KdV-NFT reliably reveals the inner nonlinear soliton structure of a propagating bore and allows to predict the far-field solitons from the near-field bore time or space series.

CRediT authorship contribution statement

Markus Brühl: Conceptualization, Software, Validation, Formal analysis, Investigation, Writing – original draft, Visualization. **Peter J. Prins:** Software, Validation, Formal analysis, Writing – review & editing, Visualization. **Sebastian Ujvary:** Methodology, Investigation, Formal analysis. **Ignacio Barranco:** Conceptualization, Methodology, Investigation, Supervision. **Sander Wahls:** Writing – review & editing, Supervision, Project administration, Funding acquisition. **Philip L.-F. Liu:** Conceptualization, Methodology, Resources, Writing – review & editing, Supervision, Project administration.

Declaration of competing interest

The authors declare the following financial interests/personal relationships which may be considered as potential competing interests: Sander Wahls reports financial support was provided by European Research Council, Markus Brühl reports financial support was provided by German Research Foundation, Philip L.-F. Liu reports financial support was provided by National Research Foundation of Singapore.

Acknowledgements

Appendix

The definition for the amplitudes A_j of the solitons is given as (Osborne and Petti [14, Eq. (17)])

$$A_j = \frac{2}{\lambda} \left(E_{\text{ref}} - E_{2j}\right), \quad 1 \leq j \leq N_{\text{sol}}, \quad E \leq E_{\text{ref}}. \tag{A.1}$$

The calculation of the soliton wave numbers K_j is based on Osborne et al. [56, Eq. (2.12)], but modified in analogy to the equation for k_k in Osborne and Segre [57, Eq. (2.10)] in order to consider the shift by the reference level E_{ref}:

$$K_j = \left(\overline{E}\right)^{1/2} = \left[0.5 \left(E_{2j+1} + E_{2j} - 2E_{\text{ref}}\right)\right]^{1/2}. \tag{A.2}$$

Furthermore, for separation of soliton and radiation spectra in the nonlinear spectra, the imaginary soliton wave numbers are plotted as

$$K_j = -\Im \left\{ \left[0.5 \left(E_{2j+1} + E_{2j} - 2E_{\text{ref}}\right)\right]^{1/2} \right\}. \tag{A.3}$$

In case of time series as input, the equations for the wavenumbers provide the frequencies Ω_j instead. The modulus for both soliton and radiation components is calculated as (Osborne [10, p. 445)])

$$m_i = \frac{E_{2i+1} - E_{2i}}{E_{2i+1} - E_{2i-1}}, \quad \text{for all } i. \tag{A.4}$$

The soliton phases Φ_j used within this paper are calculated after Prins and Wahls [46, Eq. (15)].

The variables E_n in Eqs. (A.1) to (A.4) refer to the eigenvalues of the nth ± 1-crossings of the so-called Floquet discriminant $\Delta(E)$ which is the result of the application of the Schrödinger eigenvalue problem to the analysed free-surface data. The value E_{ref} defines the threshold between the soliton and the radiation spectrum in the Floquet discriminant representation. For further details, see Osborne et al. [56, sect. 2] or, for further reading, Osborne [10, sect. 17].

Since this paper focuses on the soliton spectrum, the radiation wave parameters are not calculated here. They are given in Osborne [58, Eq. (3.22)] for the wave amplitude a_k, and in Osborne and Segre [57, Eq. (2.10)] for the wavenumber k_k. The calculation of the radiation phases φ_k is described in Osborne [10, Ch. 14].

References

[1] G.A. El, in: R. Grimshaw (Ed.), Korteweg–de Vries equation: Solitons and undular bores, in: Solitary Waves in Fluids, Advances in Fluid Mechanics, WIT Press, 2007.
[2] J.R. Apel, Oceanic internal waves and solitons, in: C. Jackson, J. Apel (Eds.), Synthetic Aperture Radar Marine User's Manual, 2004.
[3] M. Brühl, S. Wahls, I. Barranco Granged, P.L.-F. Liu, Analysis of bore characteristics using KdV-based nonlinear Fourier transform (OMAE2020-19074), 2020, http://dx.doi.org/10.1115/OMAE2020-19074.
[4] S.L. Gavrilyuk, V.Y. Liapidevskii, A.A. Chesnokov, Spilling breakers in shallow water: applications to Favre waves and to the shoaling and breaking of solitary waves, J. Fluid Mech. 808 (2016) 441–468, http://dx.doi.org/10.1017/jfm.2016.662.
[5] J.L. Hammack, H. Segur, The Korteweg–de Vries equation and water waves. Part 2. Comparison with experiments, J. Fluid Mech. 65 (1974) 289–314, http://dx.doi.org/10.1017/S002211207400139X.
[6] A.R. Osborne, in: G. Benedek, H. Bilz, R. Zeyher (Eds.), The spectral transform: Methods for the Fourier analysis of nonlinear wave data, in: Statics and Dynamics of Nonlinear Systems, Springer-Verlag, Berlin, 1983, pp. 242–261, http://dx.doi.org/10.1007/978-3-642-82135-6_22.
[7] K. Takahashi, T. Tomita, Simulation of the 2011 Tohoku Tsunami in Kuji Bay using three-dimensional non-hydrostatic numerical model, J. Jpn. Soc. Civ. Eng., Ser. B2 69 (2) (2013) I_166–I_170, http://dx.doi.org/10.2208/kaigan.69.I_166.
[8] P.A. Madsen, D.R. Fuhrman, H.A. Schäffer, On the solitary wave paradigm for tsunamis, J. Geophys. Res.: Oceans 113 (C12) (2008) http://dx.doi.org/10.1029/2008jc004932.
[9] M. Tissier, J. Dekkers, A. Reniers, P. S., A. van Dongeren, Undular bore development over a laboratory fringing reef (conference presentation), in: Coastal Engineering Proceedings (ICCE2018), 1(36), currents.53, 2018, http://dx.doi.org/10.9753/icce.v36.currents.53.
[10] A.R. Osborne, Nonlinear ocean waves and the inverse scattering tTransform, Elsevier, Amsterdam, 2010, p. 977.
[11] M. Brühl, Direct and inverse nonlinear Fourier transform based on the Korteweg–de Vries equation (KdV-NLFT) - A spectral analysis of nonlinear surface waves in shallow water (PhD thesis), TU Braunschweig, Germany, 2014, URL http://www.digibib.tu-bs.de/?docid=00058144.
[12] C.S. Gardner, J.M. Greene, M.D. Kruskal, R.M. Miura, Method for solving the Korteweg–de Vries equation, Phys. Rev. Lett. 19 (19) (1967) 1095–1097, http://dx.doi.org/10.1103/PhysRevLett.19.109.
[13] P.D. Lax, Integrals of nonlinear equations of evolution and solitary waves, Comm. Pure Appl. Math. 21 (5) (1968) 467–490, http://dx.doi.org/10.1002/cpa.3160210503.
[14] A.R. Osborne, M. Petti, Laboratory-generated, shallow-water surface waves: Analysis using the periodic, inverse scattering transform, Phys. Fluids 6 (5) (1994) 1727–1744.
[15] A.R. Osborne, The inverse scattering transform: Tools for the nonlinear Fourier analysis and filtering of ocean surface waves, Chaos Solitons Fractals 5 (12) (1995) 2623–2637.
[16] D.J. Korteweg, G. De Vries, On the change of form of long waves advancing in a rectangular canal, and on a new type of long stationary waves, Philos. Mag. Ser. 5 (39) (1895) 422–443, http://dx.doi.org/10.1080/14786449508620739.
[17] B.A. Dubrovin, Inverse problem for periodic finite-zoned potentials in the theory of scattering, Funct. Anal. Appl. 9 (1) (1975) 61–62, http://dx.doi.org/10.1007/BF01078183.
[18] B.A. Dubrovin, S.P. Novikov, Periodic and conditionally periodic analogs of the many-soliton solution of the KdV equation, Sov. Phys. JETP 40 (1975) 1058.
[19] M. Brühl, H. Oumeraci, Analysis of long-period cosine-wave dispersion in very shallow water using nonlinear Fourier transform based on the KdV equation, Appl. Ocean Res. 61 (2016) 81–91, http://dx.doi.org/10.1016/j.apor.2016.09.009.
[20] M. Brühl, M. Becker, Analysis of subaerial landslide data using nonlinear Fourier transform based on Korteweg–de Vries equation (KdV-NLFT), J. Earthq. Tsunami (JET) (2018) http://dx.doi.org/10.1142/S179343111840002X.
[21] M. Brühl, E. Büchner, H. Zhang, Amplitudes of landslide-generated impulse waves from nonlinear Fourier transform as function of the slide characteristics, in: Proc. 7th Int. Conf. on the Application of Physical Modelling in Coastal and Port Engineering and Science, Coastlab18, 2018.
[22] M. Brühl, H. Oumeraci, Analysis of soliton fission over a submerged structure using 'nonlinear Fourier transform (NLFT)', in: ICCE 2010, No. 32(2010), 2010, http://dx.doi.org/10.9753/icce.v32.waves.59.
[23] M. Brühl, H. Oumeraci, Application of 'nonlinear Fourier transform (NLFT)' for the analysis of soliton fission behind submerged reefs with finite width (OMAE2011-49668), 2011, http://dx.doi.org/10.1115/OMAE2011-49668.
[24] A. Gossel, M. Brühl, H. Oumeraci, Influence of wave and structure parameters on the transformation of solitary waves at submerged reefs using nonlinear Fourier transform (NLFT), in: Proc. 4th International Conference on the Application of Physical Modelling to Port and Coastal Protection, Coastlab2012, 2012.
[25] P.J. Lynett, P.L.-F. Liu, K.I. Sitanggang, D.-H. Kim, Modeling wave generation, evolution and interaction with depth-integrated, dispersive wave equations. COULWAVE code manual. Cornell University long and intermediate wave modeling package v. 2.0, 2008.
[26] S. Ujvary, Nonlinear analysis of bore-shaped waves from wave flume experiments (Student research project), TU Braunschweig, Germany, 2019.
[27] J.W. Miles, Solitary waves, Annu. Rev. Fluid Mech. 12 (1980) 11–43, http://dx.doi.org/10.1146/annurev.fl.12.010180.000303.
[28] G.B. Whitham, Linear and nonlinear waves, Wiley, New York, 1974, p. 635.
[29] A.R. Osborne, Behaviour of solitons in random-function solutions of the periodic Korteweg–de Vries equation, Phys. Rev. Lett. 71 (19) (1993) 3115–3118, http://dx.doi.org/10.1103/PhysRevLett.71.3115.
[30] V.I. Karpman, Non-linear waves in dispersive media, Pergamon, Oxford, 1975.
[31] M. Antonova, A. Biswas, Adiabatic parameter dynamics of perturbed solitary waves, Commun. Nonlinear Sci. Numer. Simul. 14 (3) (2009) 734–748, http://dx.doi.org/10.1016/j.cnsns.2007.12.004.
[32] L. Girgis, A. Biswas, Soliton perturbation theory for nonlinear wave equations, Appl. Math. Comput. (ISSN: 00963003) 216 (7) (2010) 2226–2231, http://dx.doi.org/10.1016/j.amc.2010.03.056.
[33] S.P. Novikov, A method for solving the periodic problem for the KdV equation and its generalizations, in: R.K. Bullough, P.J. Caudry (Eds.), Solitons, Springer, Berlin, 1980, pp. 325–338.
[34] A.R. Osborne, Soliton physics and the periodic inverse scattering transform, Physica D 86 (1995) 81–89, http://dx.doi.org/10.1016/0167-2789(95)00089-M.

[35] M. Brühl, H. Oumeraci, Nonlinear Fourier transform (NLFT) for the identification of transmitted solitons behind submerged reefs: The reconstruction of the original data (OMAE2014-24162), 2014, http://dx.doi.org/10.1115/OMAE2014-24162.

[36] M. Brühl, H. Oumeraci, Nonlinear decomposition of transmitted wave trains from soliton fission using 'nonlinear Fourier transform (NLFT)': The spectral basic components (OMAE2012-83418), 2012, http://dx.doi.org/10.1115/OMAE2012-83418.

[37] J.J. Stoker, Water waves: The mathematical theory with applications, Wiley, New York, 1957, p. 567.

[38] J.A. Liggett, Fluid mechanics, McGraw, 1994.

[39] I. Barranco, P.L.-F. Liu, Runup and inundation generated by non-decaying dam-break bores on a planar beach, J. Fluid Mech. 916, A81 (2021) http://dx.doi.org/10.1017/jfm.2021.98.

[40] R.L. Miller, Experimental determination of run-up of undular and fully developed bores, J. Geophys. Res. 73 (14) (1968) 4497–4510, http://dx.doi.org/10.1029/JB073i014p04497.

[41] H. Favre, Ondes de translation, Duno, Paris, 1935.

[42] J.S. Russell, Report on waves, Report, Report of the 14th Meeting of British Association for the Advancement of Science, York, 1844.

[43] R.G. Dean, R.A. Dalrymple, Water wave mechanics for engineers and scientists, World Scientific, Singapore, 1991, p. 353.

[44] M.J. Ablowitz, Y. Kodama, Note on asymptotic solutions of the Korteweg–de Vries equation with solitons, Stud. Appl. Math. 66 (2) (1982) 159–170, http://dx.doi.org/10.1002/sapm1982662159.

[45] G.L. Lamb, Elements of soliton theory, Pure & Applied Mathematics, Wiley-Interscience, New York, 1980.

[46] P.J. Prins, S. Wahls, Soliton phase shift calculation for the Korteweg–de Vries equation, IEEE Access 7 (2019) 122914–122930, http://dx.doi.org/10.1109/access.2019.2932256.

[47] P. Schuur, Multisoliton phase shifts in the case of a nonzero reflection coefficient, Phys. Lett. A 102A (9) (1984) 387–392, http://dx.doi.org/10.1007/BFb0073058.

[48] H. Segur, The Korteweg–de Vries equation and water waves. Solutions of the equation. Part I, J. Fluid Mech. 59 (4) (1973) 721–736.

[49] A. Galindo, P. Pascual, Quantum mechanics I, Springer-Verlag, Berlin Heidelberg, 1990, p. 430.

[50] J. Giovanangeli, C. Kharif, Y. Stepanyants, Soliton spectra of random water waves in shallow basins, Math. Model. Nat. Phenom. 13 (4) (2018) http://dx.doi.org/10.1051/mmnp/2018018.

[51] A.R. Osborne, Nonlinear Fourier analysis for the infinite-interval Korteweg–de Vries equation I: An algorithm for the direct scattering transform, J. Comput. Phys. 94 (1991) 284–313.

[52] P.J. Prins, S. Wahls, An accurate O(N^2) floating point algorithm for the Crum transform of the KdV equation, Commun. Nonlinear Sci. Numer. Simul. (ISSN: 1007-5704) 102 (2021) 105782, http://dx.doi.org/10.1016/j.cnsns.2021.105782.

[53] I. Barranco, Generation and propagation of tsunami-like bores and characteristics of the produced inundation (PhD thesis), NUS Singapore, 2021, URL https://scholarbank.nus.edu.sg/handle/10635/192622.

[54] S.J. Orfanidis, Introduction to signal processes, Prentice Hall, 2010, p. 795.

[55] G.H. Keulegan, Gradual damping of solitary waves, J. Res. Natl. Bur. Stand. 40 (1948) 15, http://dx.doi.org/10.6028/JRES.040.041.

[56] A.R. Osborne, M. Petti, G. Liberatore, L. Cavaleri, Nonlinear Fourier analysis of laboratory generated, broad-banded surface waves, in: B. Schrefler, O. Zienkeiwicz (Eds.), Computer Modelling in Ocean Engineering, Proceedings of an International Conference on Computer Modelling in Ocean Engineering, Venice, 19–23 September 1988, Balkema, Rotterdam, 1988, pp. 99–105.

[57] A.R. Osborne, E. Segre, Numerical solutions of the Korteweg–de Vries equation using the periodic scattering transform μ-representation, Physica D 44 (1990) 575–604.

[58] A.R. Osborne, Nonlinear fourier analysis, in: A.R. Osborne (Ed.), Nonlinear Topics in Ocean Physics, Proceedings of the International School of Physics "Enrico Fermi", Course CIX, Varenna on Lake Como, 26 July - 5 August 1988, vol. 109, North-Holland, Amsterdam, 1991, pp. 669–699.